

Practical and Intrinsic Predictability of Severe and Convective Weather at the Mesoscales

CHRISTOPHER MELHAUSER AND FUQING ZHANG

Department of Meteorology, The Pennsylvania State University, University Park, Pennsylvania

(Manuscript received 23 November 2011, in final form 21 June 2012)

ABSTRACT

This study explores both the practical and intrinsic predictability of severe convective weather at the mesoscales using convection-permitting ensemble simulations of a squall line and bow echo event during the Bow Echo and Mesoscale Convective Vortex (MCV) Experiment (BAMEX) on 9–10 June 2003. Although most ensemble members—initialized with realistic initial condition uncertainties smaller than the NCEP Global Forecast System Final Analysis (GFS FNL) using an ensemble Kalman filter—forecast broad areas of severe convection, there is a large variability of forecast performance among different members, highlighting the limit of practical predictability. In general, the best-performing members tend to have a stronger upper-level trough and associated surface low, producing a more conducive environment for strong long-lived squall lines and bow echoes, once triggered. The divergence in development is a combination of a dislocation of the upper-level trough, surface low with corresponding marginal environmental differences between developing and nondeveloping members, and cold pool evolution by deep convection prior to squall line formation. To further explore the intrinsic predictability of the storm, a sequence of sensitivity experiments was performed with the initial condition differences decreased to nearly an order of magnitude smaller than typical analysis and observation errors. The ensemble forecast and additional sensitivity experiments demonstrate that this storm has a limited practical predictability, which may be further improved with more accurate initial conditions. However, it is possible that the true storm could be near the point of bifurcation, where predictability is intrinsically limited. The limits of both practical and intrinsic predictability highlight the need for probabilistic and ensemble forecasts for severe weather prediction.

1. Introduction

Understanding the sources of forecast uncertainties and error growth dynamics in numerical weather prediction of squall lines, bow echoes, and other mesoscale convective systems (MCSs) may be essential in predicting severe weather, both deterministically and probabilistically. It is well documented that convective cells forming in favorable environmental conditions can be organized into a linear squall line, with subsequent bow echo formation producing damaging straight-line surface winds. This study examines the predictability and dynamics of one such event during the Bow Echo and Mesoscale Convective Vortex (MCV) Experiment (BAMEX) on 9–10 June 2003 in which two supercell storms organized into a squall line structure. Multiple

bowing segments evolved, producing damaging surface winds in eastern Nebraska and western Iowa (Davis et al. 2004). BAMEX was conducted from 20 May to 6 July 2003 across the Midwest and high plains of the United States. The major objectives of BAMEX were to observe and understand MCSs at scales ranging from those of the outflow boundaries and rear inflow jets of squall lines and bow echoes to the larger MCVs and environmental structure, to ultimately improve quantitative precipitation forecasts (QPFs) associated with these convective systems for the 6–24-h time scale (Davis et al. 2004; Done et al. 2004).

Despite recent advances in numerical weather prediction (NWP) models, the predictability of these mesoscale convective events remains unclear. Broadly speaking, there are two types of predictability issues: practical predictability and intrinsic predictability. Practical predictability is described as “the ability to predict based on the procedures currently available”, whereas intrinsic predictability is defined as “the extent to which prediction is possible if an optimum procedure

Corresponding author address: Dr. Fuqing Zhang, Department of Meteorology, The Pennsylvania State University, University Park, PA 16802.
E-mail: fzhang@psu.edu

is used" (Lorenz 1969; Zhang et al. 2006, p. 149). The practical predictability can be limited by uncertainties in both the forecast model and initial conditions. At present, these uncertainties remain sizeable, constrained by the current capability of observations, data assimilation, modeling, and computing. The intrinsic predictability is the predictability given nearly perfect knowledge of the atmospheric state and a nearly perfect forecast model (Lorenz 1969). Both practical and intrinsic predictability can be flow dependent (Lorenz 1996; Zhang et al. 2006) with expected loss of predictability during regime transition (Palmer 1993).

In a study of the 24–25 January 2000 "surprise snowstorm" by Zhang et al. (2002), it is found that insufficient model grid spacing, poor interpolation of a few key soundings during data assimilation, and realistic errors in the initial conditions (ICs) may be the key reasons for the forecast failure by operational NWP models (i.e., limit of practical predictability at the time of the storm). It has also been shown that adding small-scale and small-amplitude initial condition perturbations may lead to substantial forecast differences at the mesoscales in 24–36 h, derived from the chaotic nature of moist dynamics (i.e., intrinsic predictability of the storm is limited; Zhang et al. 2003). It was found that small-scale errors from moist processes below 100 km rapidly grew upscale due to the nonlinearity inherent in the moist processes. The effect of moist convection on the mesoscale predictability was further generalized to the idealized moist baroclinic waves in Tan et al. (2004) and Zhang et al. (2007).

A multistage error-growth conceptual model was developed in Zhang et al. (2007), finding that small-scale small-amplitude initial condition errors first grow at the convective scales and quickly saturate these scales within hours. The subsequent upscale error growth through geostrophic adjustment and/or cold pool dynamics leads to error saturation at the mesoscales with the time scale $O(2\pi/f)$. The balanced component of the saturated error at the mesoscales further grows with the large-scale background baroclinic waves, which may eventually limit the predictability at larger scales. This is consistent with more recent predictability studies with global models (Sellwood et al. 2008; Mapes et al. 2008).

The predictability of warm-season weather has been studied for flooding events over southern Texas (Zhang et al. 2006) and along the mei-yu front in China (Bei and Zhang 2007). Similar to the findings of Zhang et al. (2002, 2003) on winter cyclones, they found that small-scale error growth is strongly nonlinear and grows rapidly upscale due to moist processes, which ultimately limited the mesoscale predictability of such flooding events. The error-growth dynamics and the inherent limit of predictability of quantitative precipitation

forecasting with full-nonlinear cloud-permitting numerical models are also consistent with the recent findings of Hohenegger and Schär (2007b,a) and Clark et al. (2010). The effect of moist convection may also limit the skills of hurricane prediction, especially the intensity forecast, as shown in more recent studies by Sippel and Zhang (2008, 2010) and Zhang and Sippel (2009).

The predictability of MCSs has also been studied by Wandishin et al. (2008, 2010) using ensembles with both two- and three-dimensional model simulations by only perturbing the initial conditions in a homogenous environment in the z direction. They found similar predictability in both two- and three-dimensional simulations, with a reduction in initial-condition uncertainty improving the models' ability to maintain an MCS.

Consistent with Zhang et al. (2002, 2003) for the winter snowstorm, Clark et al. (2010) shows a larger error growth in mass-related fields and all low-level fields for springtime weather in higher-resolution convection-permitting models (4 km) versus their convection-parameterizing counterparts (20 km) for an ensemble with perturbed lateral and boundary conditions (BCs).

Most recently, Wang et al. (2012) examined the impact of microphysical scheme complexity on mesoscale predictability of warm-season convection over the central United States in cloud-permitting simulations. They found that the simplest and most complex schemes shared a similar error growth rate of initial perturbations, which further suggests the error growth is intrinsic to the nonlinearity in the moist dynamics.

The current study adopts an ensemble sensitivity analysis similar to that applied by Zhang (2005) and Hawblitzel et al. (2007) in order to understand the dynamics and predictability of the 9–10 June 2003 bow echo and squall line event during BAMEX. Done et al. (2004) suggested that the high-resolution Weather Research and Forecasting Model (WRF) runs during the BAMEX campaign for field forecasts were able to simulate the timing, location, and mode of a majority of the MCSs encountered. The success of the WRF deterministic forecasts during the BAMEX field campaign allows one to hypothesize that deterministic NWP forecasts during the May–June BAMEX period were able to consistently forecast convective-scale processes. To test this trend, this study examines one of these storms using a WRF ensemble with realistic initial condition uncertainties. Understanding the mesoscale predictability and corresponding error-growth dynamics of mesoscale forecasts is fundamental for advancing deterministic mesoscale forecasts, and it provides guidance on the design and implementation of ensemble prediction systems (Zhang et al. 2006).

An overview of the synoptic environment and storm-scale evolution is presented in section 2. A description of the model employed and the ensemble and initial conditions are described in section 3. The practical predictability and ensemble variability are described in section 4, the initial condition sensitivity experiments and the associated convective-scale error growth are discussed in section 5, and the intrinsic predictability with simulated reduction in ensemble spread is in section 6. Concluding remarks can be found in section 7.

2. Overview of the synoptic environment

During the 24-h period starting 1200 UTC 9 June 2003, a weak 300-hPa westerly jet extends across the high plains and into the Ohio River valley with predominantly zonal upper-level flow. An embedded shortwave trough over eastern Montana at 1200 UTC 9 June migrates over the northern BAMEX region by 0000 UTC 10 June (Fig. 1a), causing synoptic destabilization. Concurrently, the right entrance region of a 300-hPa jet streak is located over southern South Dakota and northern Nebraska, providing additional synoptic-scale lift. At the surface, low pressure develops ahead of the approaching shortwave, strengthens on the eastern side of the Rocky Mountains in eastern Wyoming, and moves over western Nebraska by 2100 UTC 9 June with an associated surface trough extending southwest into eastern Colorado. A southerly 850-hPa low-level jet (LLJ) in excess of 20 m s^{-1} extends through central Kansas and Nebraska ahead of the surface trough (not shown), advecting dewpoints over 15°C into northern Nebraska. The southerly LLJ and zonal flow aloft produces strong veering wind shear as indicated by the 0000 UTC 10 June Omaha, Nebraska, sounding (20 m s^{-1} of 0–6-km shear; not shown) and is conducive for supercell and squall line development (Weisman and Klemp 1982). Strong moisture advection with the aid of the LLJ produces most unstable CAPE (MCAPE) in excess of 2500 J kg^{-1} over central Nebraska. The extended trough from northwestern Kansas into south-central South Dakota by 2200 UTC 9 June provides a region of surface convergence aiding in storm genesis (Fig. 1c).

By 2200 UTC 9 June, the radar composite (Fig. 2) indicates deep convective development over south-central South Dakota, with discrete supercell development over Holt County in northeastern Nebraska. Another supercell is found at 0000 UTC 10 June over Custer County in central Nebraska. By 0100 UTC 10 June, both supercell storms had reports of strong tornadoes, sizable hail, and damaging surface winds. The discrete cells moved southeastward, with the northern cell developing into a bowing line segment by 0200 UTC

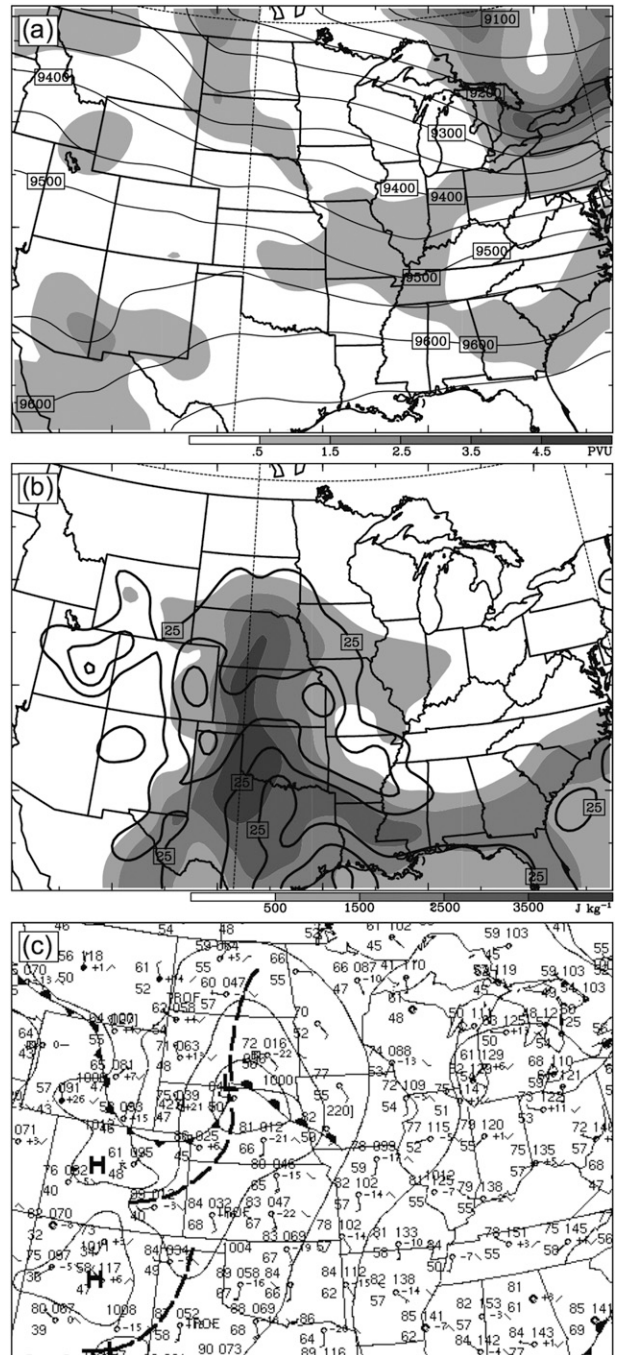


FIG. 1. GFS FNL analysis valid 0000 UTC 10 Jun (a) 300-hPa PV (shaded every 1 PVU starting at 0.5 PVU) and height (every 50 m), (b) MCAPE (shaded every 1000 J kg^{-1} starting at 500 J kg^{-1}) and MCIN (contoured every 25 J kg^{-1}), and (c) Hydrometeorological Prediction Center (HPC) surface analysis valid 0000 UTC 10 Jun.

10 June, followed shortly by the southern cell. Numerous instances of damaging surface winds in excess of 30 m s^{-1} near Lincoln and Omaha, Nebraska, were reported to the local National Weather Service (NWS)

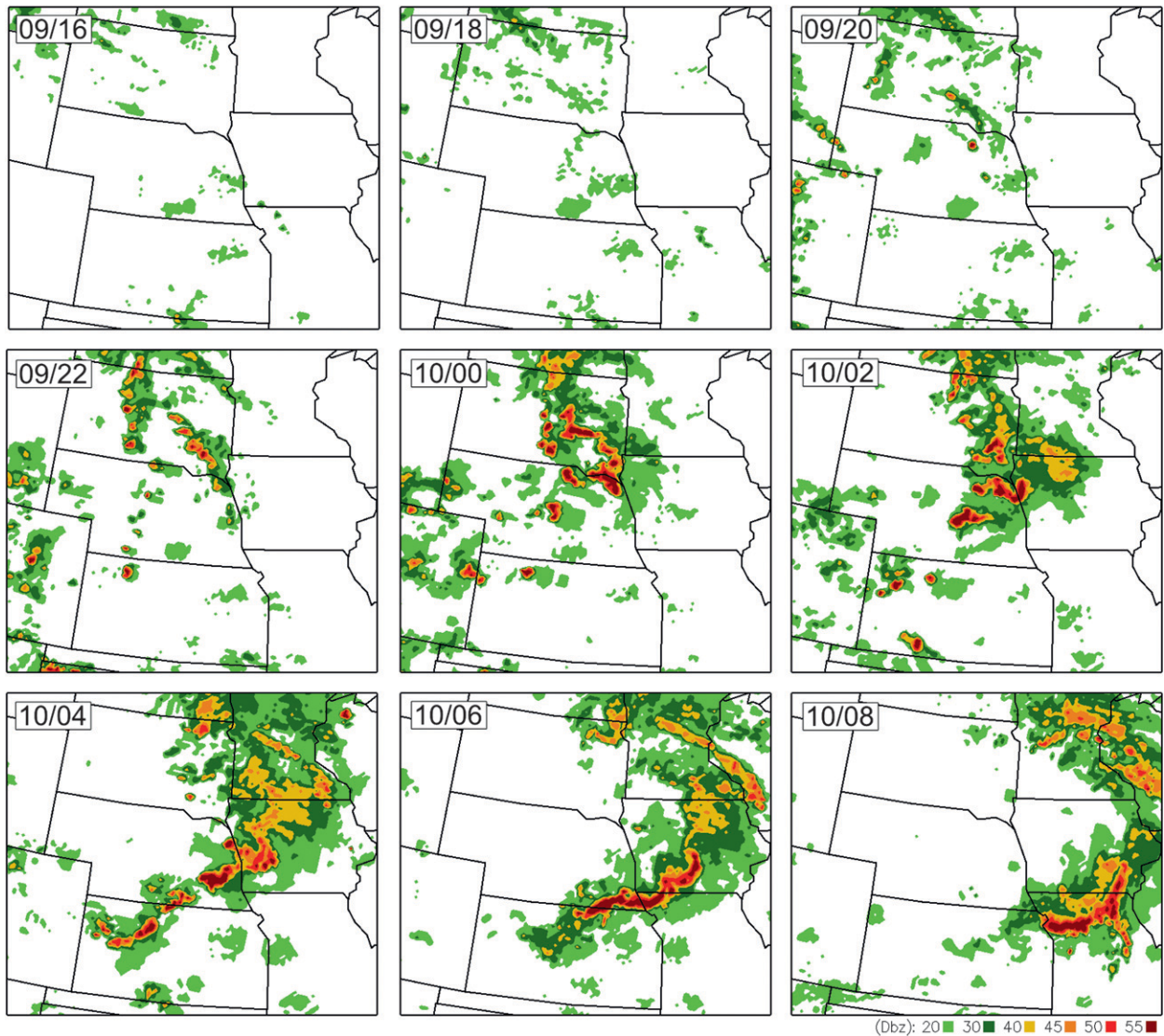


FIG. 2. Composite radar reflectivity (dBZ) observed at 1600, 1800, 2000, and 2200 UTC 9 Jun 2003 and 0000, 0200, 0400, 0600, and 0800 UTC 10 Jun from the Plymouth State University weather archive.

office between 0300 and 0600 UTC 10 June. The two discrete cells merged into one 350-km bowing line structure over southwestern Iowa by 0600 UTC 10 June.

3. Experimental design

This study utilizes the fully compressible, nonhydrostatic mesoscale WRF version 2.2 (Skamarock et al. 2005). The forecast model is initialized at 1200 UTC 9 June 2003 and integrated for 24 h. Four domains are employed, three of them two-way nested, with horizontal grid spacing of 90, 30, 10, and 3.3 km, as indicated in Fig. 3. There are 64×45 horizontal grid points in the largest domain (D01) and 297×258 horizontal grid

points in the smallest domain (D04). D04 is intended to cover the northwestern BAMEX region of interest to capture the evolution of the supercell and subsequent bow echo and squall line. All four domains utilize 27 vertical terrain-following sigma levels with a model top of 100 hPa, the WRF Single-Moment 6-Class Microphysics Scheme (WSM6) with graupel (Hong et al. 2004), and the Yonsei State University (YSU) planetary boundary scheme (Noh et al. 2003). The Grell-Dévényi cumulus scheme (Grell and Dévényi 2002) is employed for D01 and D02 given the coarse resolution of these domains. D03 and D04 are convective permitting and hence have no cumulus parameterization (Bryan et al. 2003). The Rapid Radiative Transfer Model (RRTM)

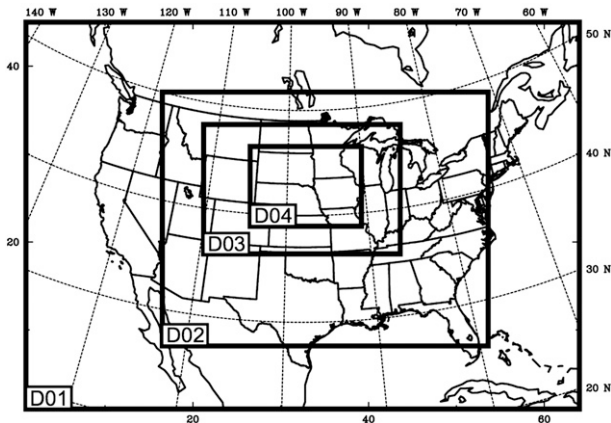


FIG. 3. Schematic of domains used in the study with resolutions D01 = 90 km, D02 = 30 km, D03 = 10 km, and D04 = 3.3 km.

longwave radiation and Dudhia shortwave radiation schemes are employed for all four domains.

This study utilizes a 40-member ensemble initialized with the ensemble Kalman filter (EnKF) analysis at 1200 UTC 9 June generated during a month-long data assimilation experiment spanning the month of June 2003, as reported in Meng and Zhang (2008b). Only quality-controlled radiosonde observations are assimilated every 12 h in D02, since an earlier study of Meng and Zhang (2008a) found only marginal benefit gained through the assimilation of additional data from surface and profiler observations. Meng and Zhang (2008b) further demonstrated that the 12–72-h WRF forecasts of D02 initialized from the control EnKF analysis consistently outperforms the forecast initialized from the WRF three-dimensional variational data assimilation (3DVar) analysis (which assimilates the same radiosondes as the EnKF) and the WRF forecasts initialized from the $0.5^\circ \times 0.5^\circ$ National Centers for Environmental Prediction Global Forecast System Final Analysis (NCEP GFS FNL), which assimilated operational observations including satellite data.

The initial and boundary conditions at 0000 UTC 1 June were generated with balanced perturbations randomly drawn from the WRF 3DVAR background uncertainty. D01 for the subsequent analysis and forecast cycles was regenerated every 12 h using the GFS FNL analyses that were perturbed with the 3DVAR background uncertainties, and the initial conditions of D02, D03, and D04 are recycled from the posterior of the EnKF. D02 is one way, while D03 and D04 are two-way nested. The initial conditions for the 9–10 June 2003 ensemble forecast study were the EnKF posterior for each ensemble member at 1200 UTC 9 June, with no further data assimilation performed during the 24-h period of focus. For further information on the EnKF

and WRF 3DVAR, and observation quality control and verification techniques, one is directed to Meng and Zhang (2008a,b), which provide the initial conditions for the ensemble simulations examined herein.

4. Ensemble performance and practical predictability

The single deterministic WRF runs were used during the BAMEX campaign to provide high-resolution (4-km horizontal grid spacing) forecasts of the region. Many of the forecasts did well in predicting the mode, temporal, and spatial characteristics of storms, notably the 9–10 June 2003 squall line and bow echo event (Done et al. 2004). The same is true for this study's control forecast shown in Fig. 4, initialized with the mean EnKF analysis at 1200 UTC 9 June. The forecast captures many of the salient features of this squall line and bow echo event in terms of structure and relative evolution (Fig. 2 vs Fig. 4). This section will examine the practical predictability of the storm.

a. Ensemble variability

The 40-member ensemble initialized with the EnKF perturbations provided a wide variety of forecasts. The initial ensemble spread has a smaller RMSE in U , V , and T compared with the corresponding NCEP GFS FNL, and the 12-h prior ensemble spread is broadly consistent with the 12-h forecast error averaged over the entire month of June (Meng and Zhang 2008b). The posterior ensemble used to initiate this study's forecasts at 1200 UTC 9 June has a spread less than the error of both the 12-h prior and the corresponding NCEP GFS FNL, and thus the initial condition uncertainties represented by the ensemble are considered realistic.

A mosaic of 20 members depicting D04 over the BAMEX region at 0600 UTC 10 June (18 h into the forecast) is shown in Fig. 5. This time was chosen because it depicts the best subjectively chosen representation of different storm modes within the ensemble. From top left to bottom right, the images show an assortment of ensemble members ranging from full squall lines with bowing sections to back-building mesoscale convective systems. The selection is a representative sample of the various storms in the ensemble. Many members produced strong squall lines but were out of phase with observations in terms of spatial location or the temporal progression of the line. The model also produced members that do not produce squall lines but instead generate lines of discrete propagating cells, back-building mesoscale convective systems, and/or small convergent convective lines that have slight bowing characteristics. The small spread of the initial conditions

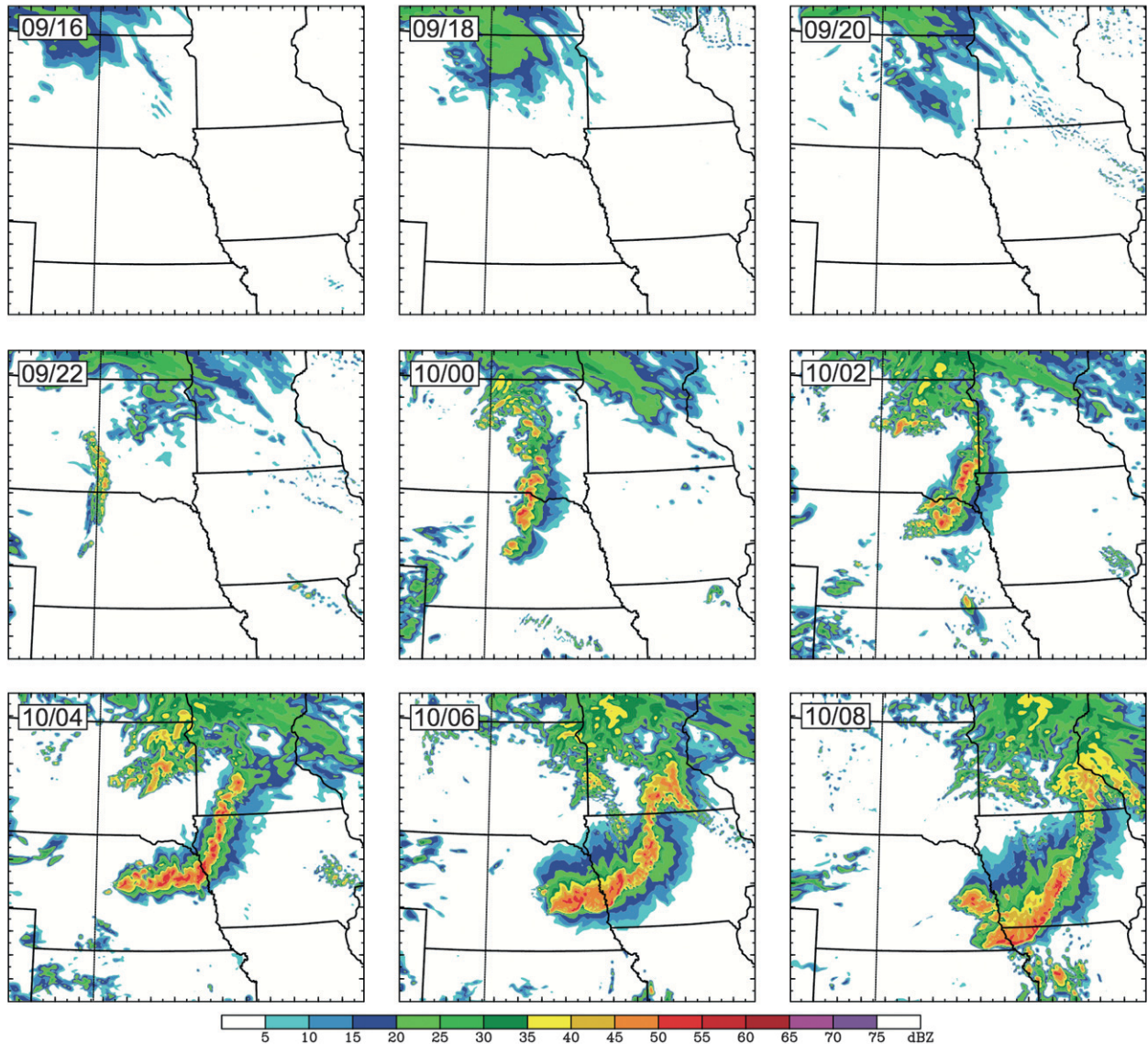


FIG. 4. Simulated radar reflectivity (shaded every 5 dBZ) for the deterministic forecast initialized with the EnKF mean analysis from 1600 UTC 9 Jun every 2 h until 0800 UTC 10 Jun.

and striking variability in storm mode is a strong indicator of a chaotic divergence (and associated large forecast error growth) of the ensemble members.

A subjective analysis of the members compared with observations was performed with multiple iterations, incorporating more details based on the previous iteration shortcomings. The final criterion to subjectively compare with observations was determined to be storm mode (squall line, bow echo, and other MCS), spatial phasing, temporal phasing, and simulated reflectivity coverage northeast of the surface low. Several human participants, two research scientists and three graduate students, applied this criterion using a numeric rank

based on the prescribed criterion to all ensemble members and generated a consensus for a GOOD, FAIR, and POOR classification. After ranking the members, a subsequent grouping into 10 GOOD, 20 FAIR, and 10 POOR was performed to focus the analysis on the 10 GOOD and 10 POOR representations of the actual storm, identifying two distinct storm modes. The mosaic of Fig. 5 begins with 5 randomly selected GOOD members, ends with 5 randomly selected POOR members, and fills the middle with 10 randomly selected FAIR members. Given the difficulties in objectively verifying storm-scale feature-based NWP forecasts, our subjective analysis provides an

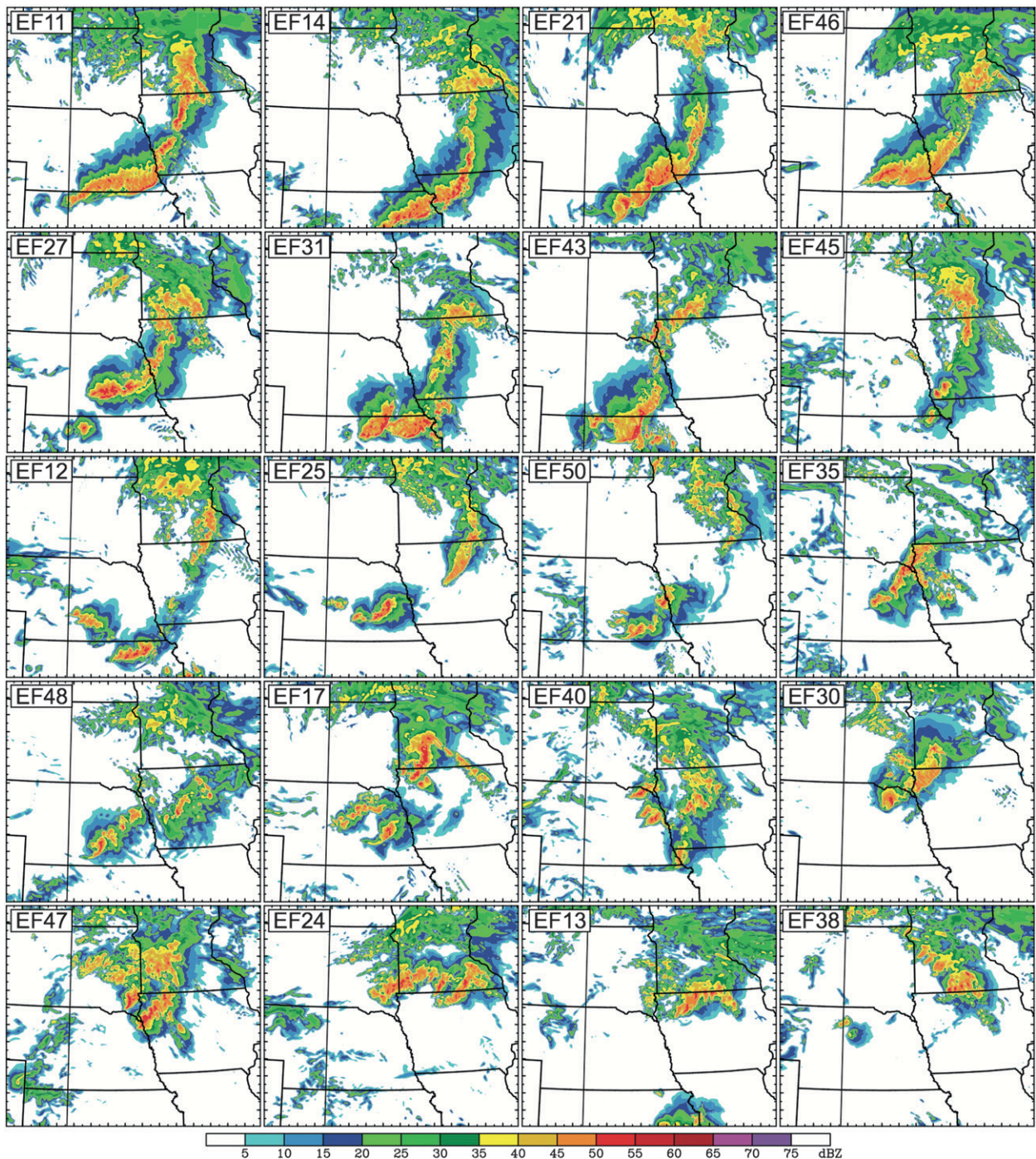


FIG. 5. Simulated radar reflectivity (shaded every 5 dBZ) for 20 ensemble members at 0600 UTC 10 Jun, subjectively sorted from squall line to non-squall line storm modes.

effective method for classifying the ensemble member's representation of the observed event.

Figure 6 compares a GOOD member with a POOR member of the ensemble, showing EF11 having a strong squall line and bow echo and EF38 having a back-building MCS. The convective development depicts two

separate storm evolutions, characteristic of the GOOD and POOR groups in the ensemble. The top panels show a clear squall line and bow echo in member EF11 by 0400 UTC 10 June, while member EF38 in the bottom panels develops only a line of discrete convective cells that propagate parallel to the warm front. Somewhere in

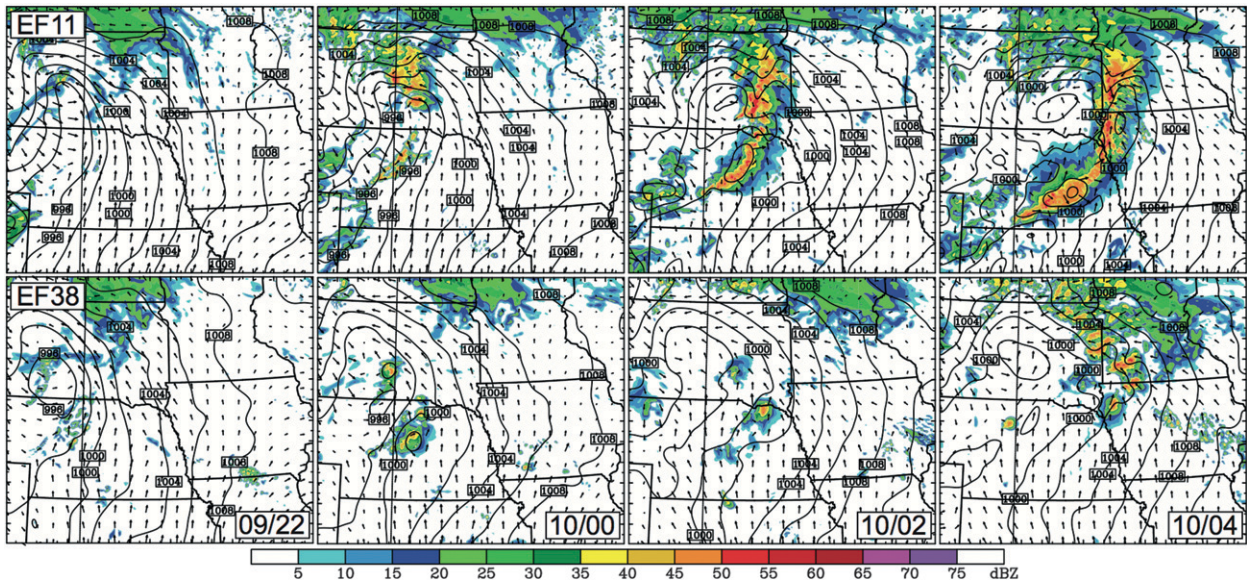


FIG. 6. Simulated radar reflectivity (dBZ), sea level pressure (hPa), and surface wind vectors for (top) EF11 and (bottom) EF38 from 2200 UTC 9 Jun to 0400 UTC 10 Jun.

the evolution—particularly between 0000 and 0200 UTC 10 June—a clear divergence in solutions occurs.

A strong shortwave trough over southern Montana at 1200 UTC 9 June (not shown) is evident in the analysis field, with the GOOD member average exhibiting a stronger upper-level trough (~ 30 m lower in 300-hPa geopotential height in Fig. 7a) than the POOR member average. A spatial trough axis lag for POOR members is evident by the dipole seen in all of the difference fields in Fig. 7 and persists for the entire forecast period. The difference between the GOOD and POOR member troughs becomes statistically significant by 1800 UTC 9 June and maintains significance through 0000 UTC 10 June. The stronger trough produces variability in the strength of the associated surface low with a statistically significant strength difference, GOOD members about 1 hPa stronger, between 1800 UTC 9 June and 2100 UTC 10 June. The location of the surface low over the northern Nebraska region is shifted farther east for GOOD members, evident by the broad area of low-pressure difference in Fig. 7b over eastern Nebraska. By 0200 UTC 10 June, the GOOD members' upper-level trough has moved over western South Dakota and a more collocated maximum in sea level pressure difference between GOOD and POOR members is evident over western Iowa (Fig. 7c). The difference in shortwave trough strength and placement is hypothesized to cause the surface low strength and spatial location differences between GOOD and POOR members. The higher amplitude trough and farther east placement of the surface low for GOOD members effects the local characteristics

of surface and 850-hPa winds, temperature, and moisture. These differences are believed to be a key factor for a divergence of the ensemble into separate modes, consistent with another BAMEX case study, by Hawblitzel et al. (2007).

Figure 8 displays the environments of the GOOD and POOR member averages at two separate times, directly following convective initiation at 2200 UTC 9 June and after storm maturation at 0200 UTC 10 June. The left panels show the simulated reflectivity, sea level pressure, and surface wind vectors; the center panel shows the MCAPE, most unstable layer convective inhibition (MCIN), and 300-hPa geopotential heights; and the right panels show the 850-hPa wind vectors and wind speed.

Convection initiates just to the east of the surface low after 2100 UTC 9 June, and by 2200 UTC 9 June, stronger reflectivity is evident by the GOOD members in central Nebraska where observations track the storm development (Fig. 2). At 2200 UTC 9 June, the GOOD members initiate in a more unstable environment with the MCAPE values greater than 1000 J kg^{-1} , less MCIN directly to the east, and a stronger southerly flow of $10\text{--}12 \text{ m s}^{-1}$ intersecting the convection. The POOR members initiate convection in areas of lower MCAPE ($<1000 \text{ J kg}^{-1}$), with larger MCIN directly to the east and a weaker southerly jet of $8\text{--}10 \text{ m s}^{-1}$. The GOOD members have a larger area of low pressure extending into central Nebraska and stronger southerly winds advecting larger MCAPE values farther north, making the environment more favorable for squall line development and maintenance in the northern portion of

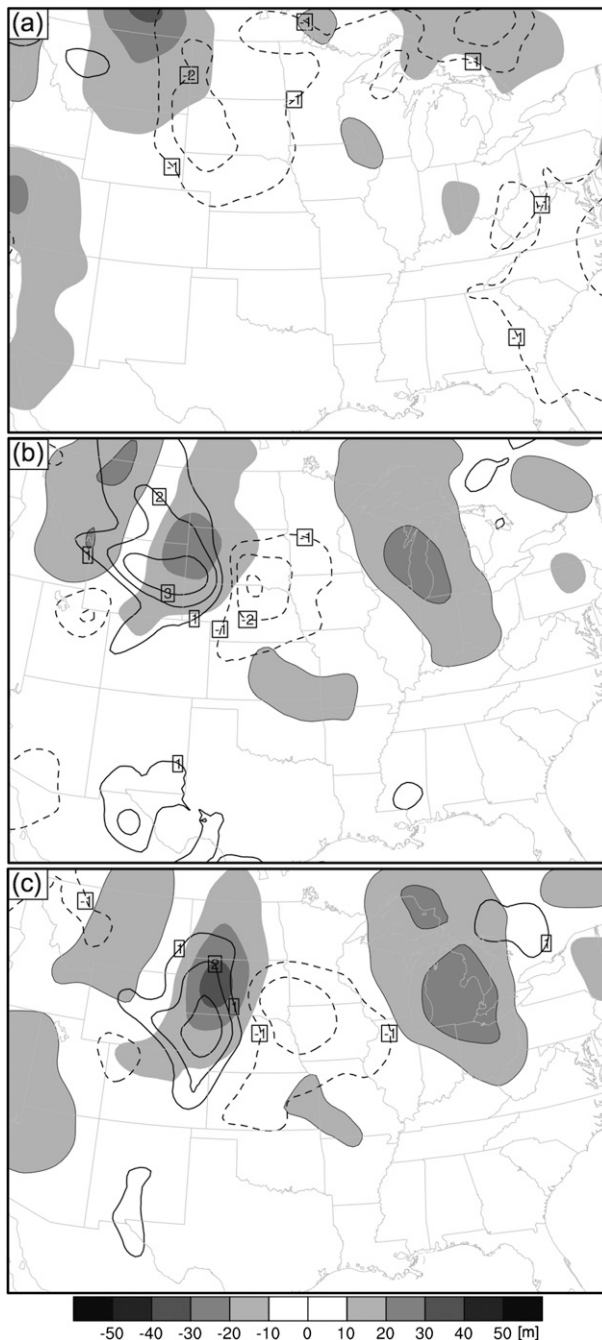


FIG. 7. Difference fields (GOOD average minus POOR average) for sea level pressure (contoured every 1 hPa; dashed for negative values) and 300-hPa geopotential height (contoured and filled every 10 m; no contour line for negative values) for D02 at (a) 1200 UTC 9 Jun, (b) 2200 UTC 9 Jun (postconvective initiation), and (c) 0200 UTC 10 Jun (postmaturation of storm mode).

Nebraska. Conversely, the weaker surface low associated with the POOR members is associated with a weaker southerly LLJ and moisture advection, creating a less favorable environment for linear MCS development.

By 0200 UTC 10 June, the simulated reflectivity for the averages of the GOOD and POOR members (first column in Fig. 8) clearly shows a difference in convection and associated storm mode. The GOOD members have a linear convective feature draped across central Nebraska, while the POOR members' reflectivity portrays less convective organization. The third column in Fig. 8 indicates that the 850-hPa winds are stronger ahead of the linear feature in the GOOD members (south-southwesterly at $18\text{--}20\text{ m s}^{-1}$) versus the POOR members (southerly at about 16 m s^{-1}). The position of the surface low for the POOR members and the lack of convection ahead of the surface trough allow surface winds to intersect the convection in the northern portion of the domain on the southern and western flanks, generating a back-building MCS mode. A key mechanism is causing development of the southern flank squall line for the GOOD members, which is discussed in section 5.

b. Ensemble error growth

The error growth and predictability of the squall line and bow echo can be examined and quantified by tracking the ensemble spread over time using the difference total energy (DTE) defined in Zhang (2005) as

$$\text{DTE} = \frac{1}{2}(u'u' + v'v' + kT'T'), \quad (1)$$

where the primes denote the difference between each ensemble member and the ensemble average (or another ensemble member), and $k = C_p T_r^{-1}$ ($C_p = 1004.9\text{ J kg}^{-1}\text{ K}^{-1}$ and $T_r = 270\text{ K}$, the reference temperature). The root-mean difference total energy (RMDTE) is then calculated from Eq. (1) as the square root of the average in either the horizontal (summing in the vertical) or the vertical (summing in the horizontal) of the DTE of all ensemble members (equations not shown).

Figure 9 shows the horizontal RMDTE for D04 for the full ensemble and the ensemble average every 2-h starting at 2200 UTC 9 June, along with those at the initial time and at 1800 UTC 9 June. The initial RMDTE from the EnKF analysis is approximately $2\text{--}3\text{ m s}^{-1}$ for the majority of the model domain. The ensemble spread remains steady from initial values through 1800 UTC 9 June, when the shortwave trough and associated surface low drive differences in the western portion of the domain. The most significant spread occurs at the onset of convection in central Nebraska at approximately 2200 UTC 9 June, where values jump to nearly 5 m s^{-1} in the area of convective initiation. This spread continues to increase steadily through 1000 UTC 10 June to values in excess of 9 m s^{-1} . It is interesting to note that the squall

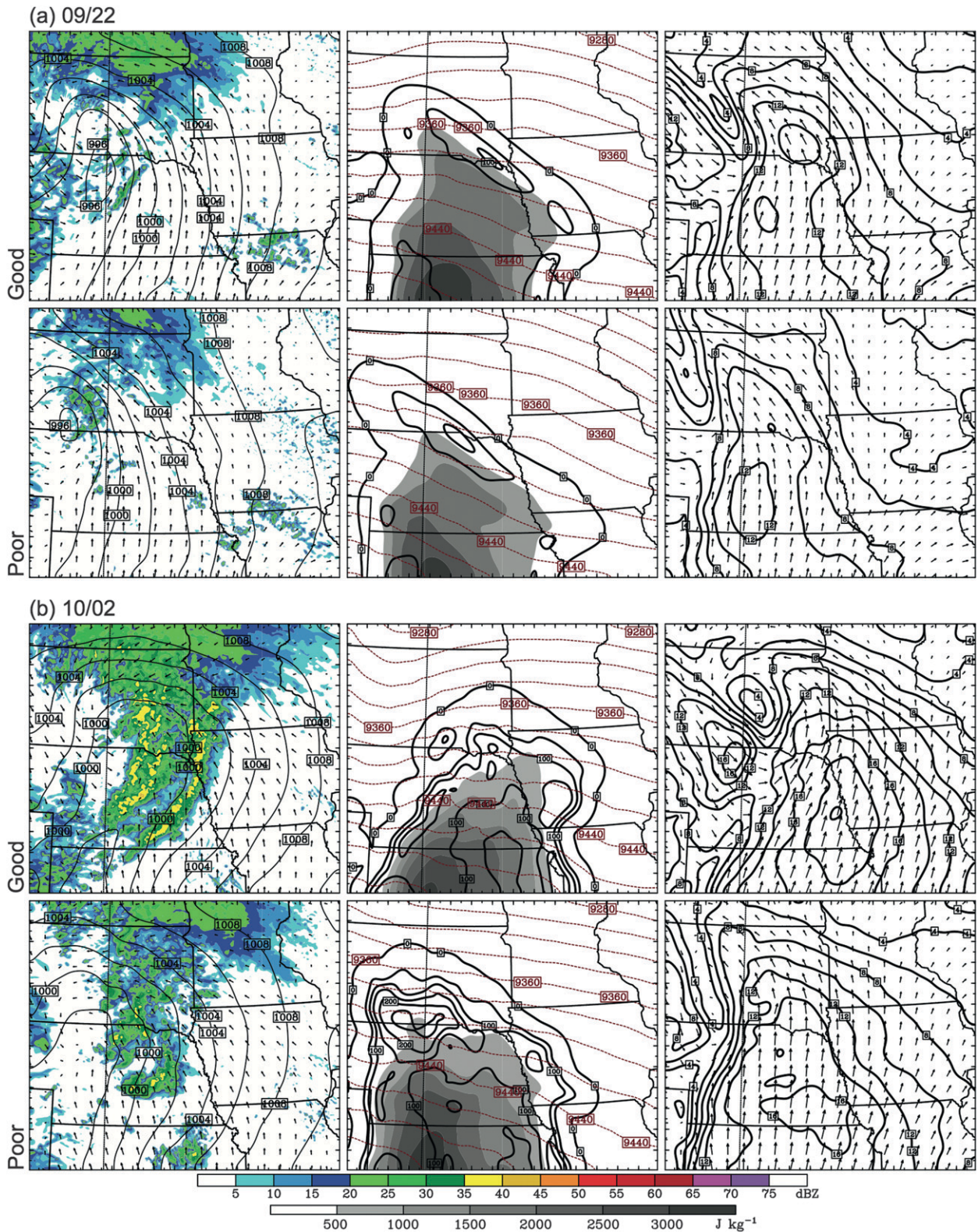


FIG. 8. Environments of the GOOD and POOR member averages at (a) 2200 UTC 9 Jun (postconvective initiation) and (b) 0200 UTC 10 Jun (postmaturation of storm mode). (left) Simulated reflectivity (contoured every 5 dBZ), sea level pressure (contoured every 2 hPa), and surface wind vectors. (middle) MCAPE (shaded every 500 $J kg^{-1}$), MCIN (contoured every 50 $J kg^{-1}$), and 300-hPa geopotential heights (contoured every 20 m). (right) 850-hPa wind vectors and wind speed (contoured every 2 $m s^{-1}$).

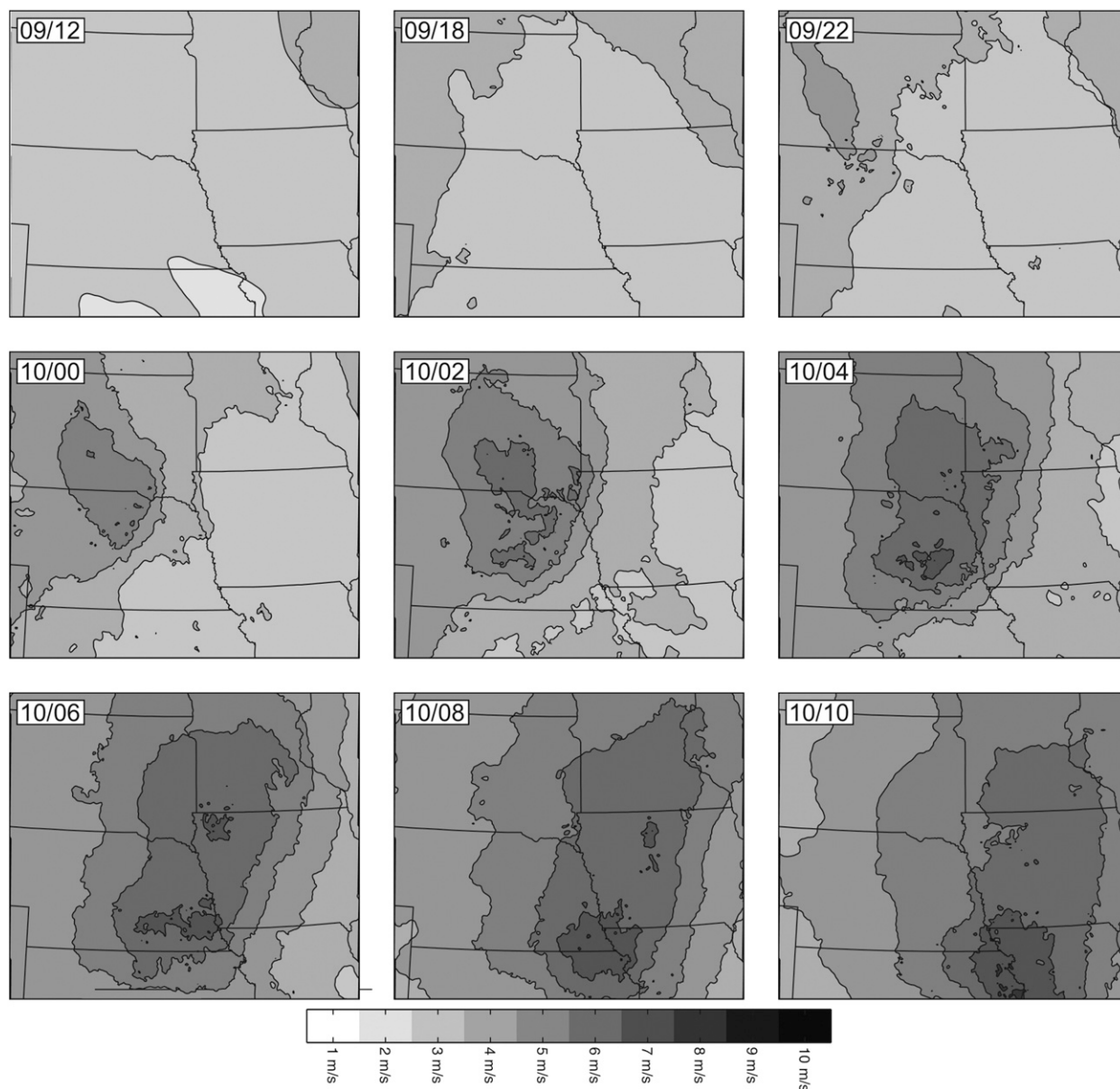


FIG. 9. Horizontal RMDTE showing the ensemble spread of the full 40-member ensemble and the full ensemble member average (shaded every 1 m s^{-1}) from 1200 UTC 9 Jun 2003 to 1000 UTC 10 Jun.

line can be detected in the error growth plot, especially in the southeastern region of Nebraska by 0600 UTC 10 June. The RMDTE coincides very well with the strong difference in the storm modes and squall line structure between members in Fig. 5. The divergence in solutions is evident by 0600 UTC 10 June in Fig. 9, with two distinct areas of large error growth. The largest error growth is in the vicinity of moist convection, which is consistent with the findings of Zhang et al. (2003) and Zhang (2005).

The vertical profile of horizontally averaged RMDTE between the full ensemble and the ensemble average is

shown in Fig. 10a with vertical profiles every 2 h starting at 2200 UTC 9 June, along with those at the initial time and at 1800 UTC 9 June. The pattern of the RMDTE is consistent with previous findings by Hawblitzel et al. (2007) and Zhang (2005), with the error growth at the approximately 1.5 km amplifying throughout the forecast period, especially after convection initiation. This indicates convection had a significant impact on the distribution of RMDTE. Between 1200 and 1800 UTC 9 June, a small jump from about 1.5 to 2.5 m s^{-1} in spread is evident at about 1.5 km, which is a signal of the moist

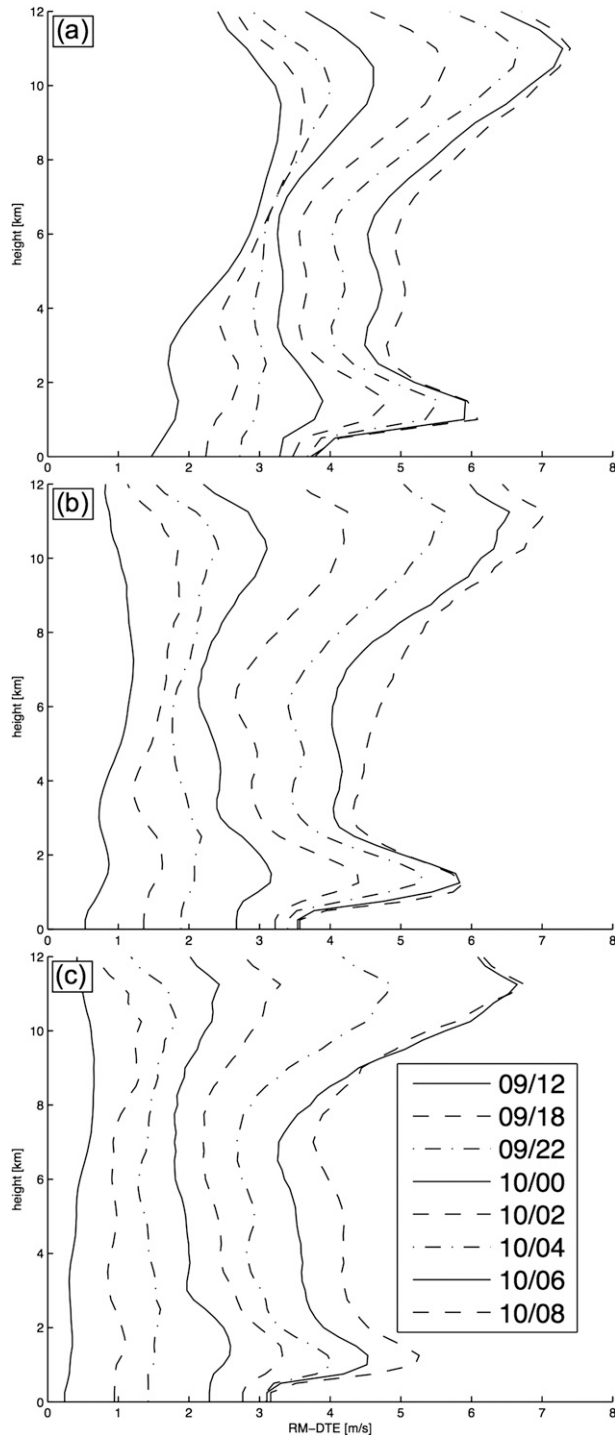


FIG. 10. Vertical RMDTE (m s^{-1}) between (a) all 40 ensemble members, (b) OKTO0 and OKTO8, and (c) OKTO4 and OKTO5 and the full ensemble member average shown at select times from 1200 UTC 9 Jun to 0800 UTC 10 Jun.

convection in the northern domain. The precipitation occurring in the northern part of the domain is driven by the synoptic destabilization associated with the short-wave trough and surface low. The low-level peak in RMDTE is located where the largest differences in temperature occur for strong convection. The large jump at 1.5 km from 2200 UTC 9 June to 0000 UTC 10 June (from about 3 to 4 m s^{-1}) signifies the beginning of strong convection in the southern portion of the domain, with a subsequent increase to 6 m s^{-1} by 0600 UTC 10 June. There is a large peak of about 7.5 m s^{-1} by 0900 UTC 10 June centered at 10 km in the upper troposphere. This peak is largely due to the geospatial displacement of the upper-level shortwave trough (which leads to a large difference in U and V) between members along with the large vertical gradient in temperature near the tropopause. The exclusion of density effect in the DTE calculation may have also contributed to the peak of DTE in the upper troposphere. The DTE analysis in Fig. 9 shows the horizontal areas of the largest error growth are associated with the divergence in moist convection between GOOD and POOR, with Fig. 10 confirming the error growth at the appropriate vertical level. A more in-depth look at the processes that lead to forecast divergence is presented in the following section.

5. Sensitivity to small IC uncertainties and intrinsic predictability

a. Overview of the sensitivity experiments

Nine additional sensitivity forecasts, from OKTO0 to OKTO8, are conducted to examine the intrinsic limit of predictability of this event. These 24-h WRF forecasts are initialized by linearly averaging all prognostic variables in the initial conditions of the 10 GOOD members and 10 POOR members with a specified weight. OKTO0 and OKTO8 are defined as the nonweighted average of the 10 GOOD members and 10 POOR members, respectively, and OKTO1 through OKTO7 are weighted averages of the GOOD and POOR members. These linear averages are created by the same manner as the EnKF mean analysis, except that the EnKF mean analysis is an average of all ensemble members. Similar initial imbalances can be detected for the forecasts initiated with the ensemble averages as those from the individual ensemble members or from the mean EnKF analysis. The averages of the GOOD and POOR members are meant to ensure representativeness of the southern squall line developing and nondeveloping storm modes in the original ensemble.

The initial condition of each sensitivity forecast contains a fraction of OKTO0 and OKTO8 initial conditions, the weighting generated using Eq. (2):

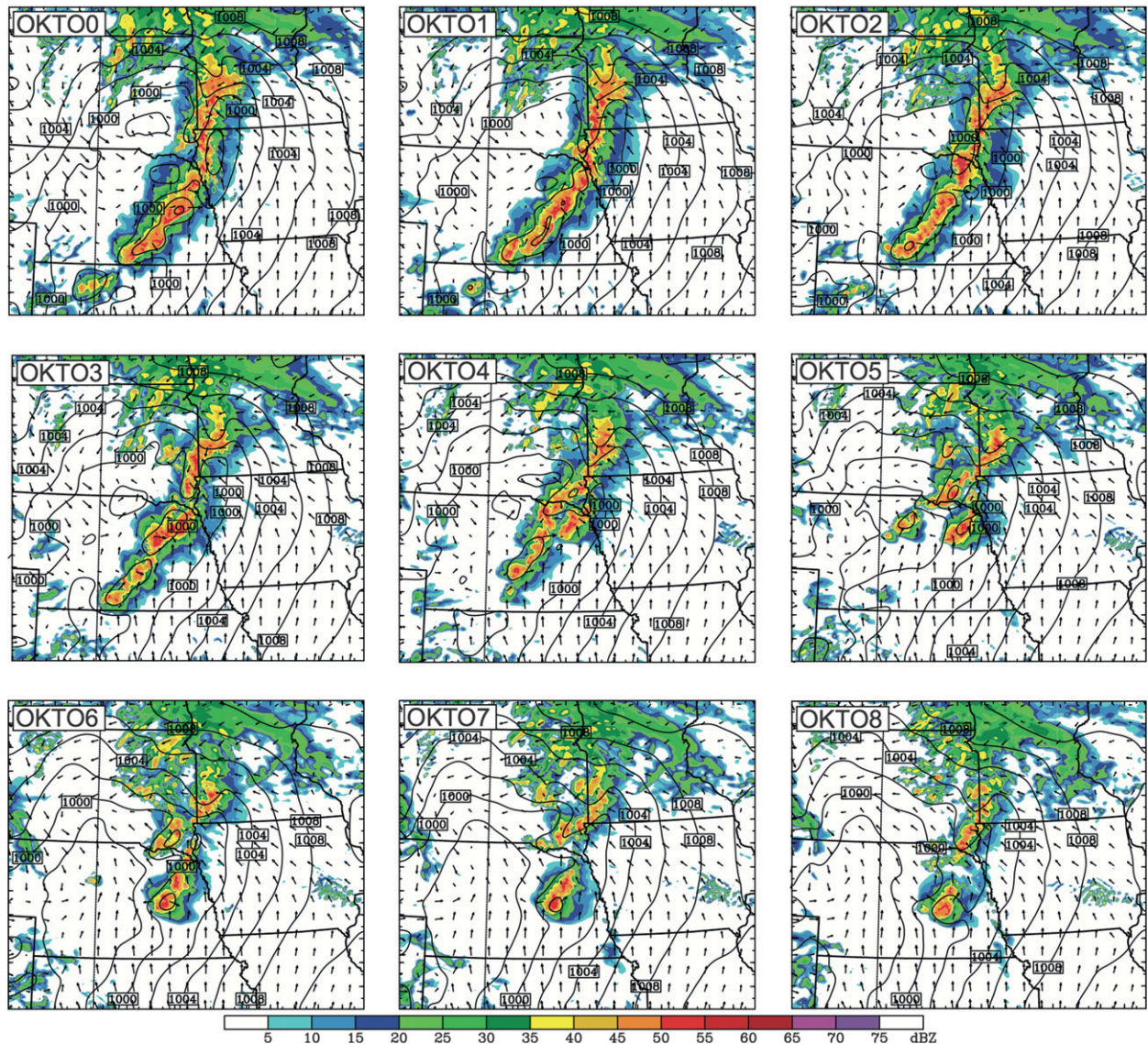


FIG. 11. Simulated radar reflectivity (shaded every 5 dBZ), sea level pressure (contoured every 2 hPa), and surface wind vectors for linearly averaged sensitivity forecasts (OKTO0 through OKTO8) at 0400 UTC 10 Jun.

$$\text{OKTOX} = \frac{1}{8} [(8 - X) \times \text{OKTO0} + X \times \text{OKTO8}], \quad (2)$$

where X indicates the sensitivity experiment number. As a fraction of the initial condition difference between OKTO0 and OKTO8, the difference between OKTO0 and OKTO4 is one-half, between OKTO0 and OKTO2 is one-quarter, and between OKTO0 and OKTO1 is one-eighth, with the other members following the same division properties. DTE is a square function, such that reductions in initial condition differences between OKTO0 and OKTO8 of one-half, one-quarter, and one-eighth

subsequently reduces the initial DTE fields by one-quarter, one-sixteenth, and one-sixty-fourth the initial difference total energy, respectively.

Figure 11 tiles the simulated reflectivity for the nine forecasts at 0400 UTC 10 June, which mimics the variability seen in the original ensemble shown in Fig. 5. There is a trend from OKTO0 to OKTO8 toward decreasing squall line formation in the southern portion of the domain. Analyzing the evolution of each forecast, a clear divergence between the southern squall line development is evident between members OKTO4 and OKTO5. The small differences in the ICs are manifesting themselves with (without) convective development in the

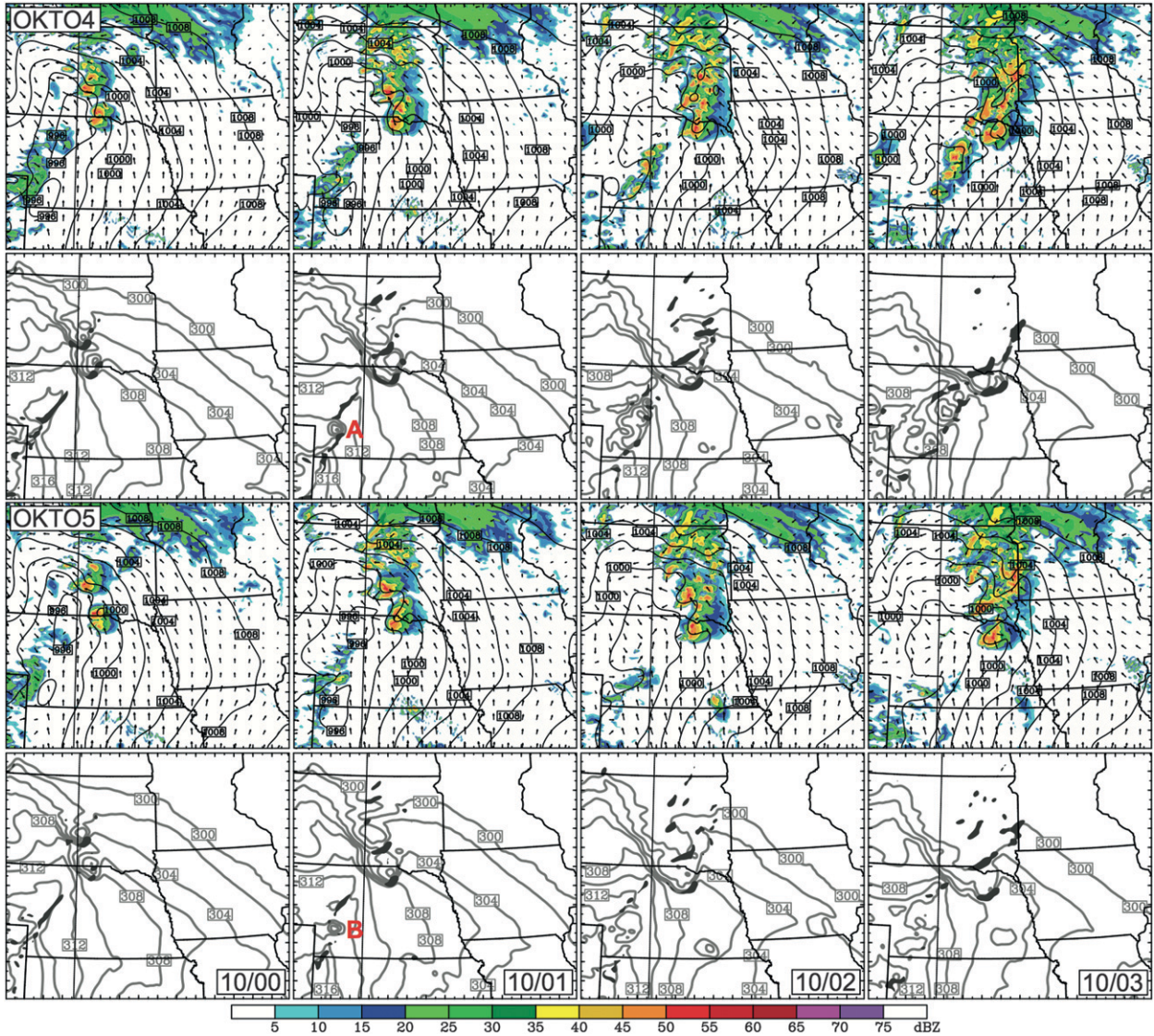


FIG. 12. Simulated radar reflectivity (shaded every 5 dBZ), sea level pressure (contoured every 2 hPa), and surface wind vectors for (first row) OKTO4 and (third row) OKTO5. Surface virtual potential temperature (contoured every 2 K) and 700-hPa vertical velocity (solid fill $>0.5 \text{ m s}^{-1}$) for (second row) OKTO4 and (fourth row 4) OKTO5 from 0000 UTC to 0300 UTC 10 Jun. Letters A and B on second and fourth rows indicate the cold pools of focus where differences in convective development help distinguish southern squall line formation.

southern portion of OKTO4 (OKTO5). This is subjectively defined as a bifurcation point, or the dividing line between the OKTO0 (GOOD—developing) and the OKTO8 (POOR—nondeveloping) flow regimes.

Figure 12 illustrates the temporal change of the simulated reflectivity, sea level pressure, and surface wind vectors (first and third rows) along with surface virtual potential temperature and vertical velocity (second and fourth rows) for the two bifurcating members, OKTO4 and OKTO5. The panels start at 0000 UTC 10 June following convective initiation in the northern portion of the domain and proceed until 0300 UTC 10 June,

corresponding to a difference in southern storm mode. Around 0100 UTC 10 June, a difference in convection (indicated by convection to the west of points A and B in Fig. 12, second and fourth rows) moving out of northeastern Colorado has an impact on the squall line development. The convection from northeastern Colorado aids in the development of the squall line in OKTO4 but not in OKTO5. The initial condition difference between OKTO4 and OKTO5 is nearly an order of magnitude smaller than realistic analysis uncertainties, and the subsequent (sub)synoptic environments in OKTO4 and OKTO5 are very similar in northeastern Colorado,

suggesting small-scale error grows upscale in modifying the evolution of convection in northeastern Colorado.

b. Moist processes and error growth: Convective scale

It has been shown in previous studies (Zhang et al. 2002, 2003, 2007; Hawblitzel et al. 2007) that moist convection produces small-scale errors that start as subconvective-scale differences and grow upscale to affect mesoscale development. This is a complement to the recent study of Zhang and Sippel (2009), noting that moist convection altered the cold pool strength of a developing tropical depression, which subsequently diverges solutions into forming and nonforming hurricanes. The previous study parallels and helps solidify the processes occurring with the convection over northeastern Colorado.

Examining the second and fourth rows in Fig. 12 more closely, the corresponding simulated reflectivity to points A and B indicate a clear difference from 0100 UTC 9 June to 0200 UTC 10 June. OKTO4 has a larger extent of stronger simulated reflectivity at 0100 UTC 10 June to the west of point A that increases in magnitude (>40 dBZ) by 0200 UTC 10 June. This is not evident with the convection west of point B in OKTO5. The associated simulated reflectivity at 0100 UTC 10 June is weaker and becomes marginal by 0200 UTC 10 June. In other words, a threshold has been reached in OKTO4 (but not in OKTO5) that maintains stronger convection near point A.

The convective initiation thresholds at localized grid points are related to the stability of the atmosphere and surface lift associated with surface mesoscale boundaries. If substantial lift is created to move a surface air parcel above its level of free convection (LFC), convection will initiate and moist processes will occur. For the forecast divergence seen between OKTO4 and OKTO5, the surface lift ahead of a cold pool is conjectured to be a threshold or an on-off switch for the subsequent convective triggering. The small-scale small-amplitude differences lead to differences in parameterized microphysics¹ that modify the cold pool strength and extent for the convection moving out of northeastern Colorado. The difference in the strength of the cold pools and the subsequent convergence and lift along the boundary cause a cascading upscale effect, altering the timing, location, and strength of subsequent convective cells.

At 0000 UTC 10 June, localized small-scale cold pools associated with OKTO4 are marginally stronger (~ 2 K) located to the west of point A compared with OKTO5. An expansive updraft is evident on the southern flank of the cold pool (dark shading), which helps to maintain the cold pool strength. The stronger cold pool generates convergence along the surface boundary, strong enough to trigger further convection and propagate the system to the east. Minimal convection is present with the associated cold pool in OKTO5 to the west of point B, not providing a mechanism for cold pool reinforcement and thus a weakening of the cold pool.

The cold pool and associated convection in OKTO4 propagates through the surface trough, maintaining and initiating new cells and triggering strong convection on its leading edge in the favorable high CAPE environment. The strong low-level southerly winds on the eastern side of the cell and high CAPE environment aid in the explosive convection seen between 0100 and 0300 UTC 10 June, subsequently developing the southern squall line in OKTO4. This is consistent with findings from idealized simulations of Wandishin et al. (2008, 2010), which showed that CAPE and wind shear along with midlevel moisture have an impact on the maintenance of the MCS.

To explore the effect of the large-scale forcing and cold pools on the divergence of the members, various sensitivity experiments were performed on OKTO0, OKTO4, OKTO5, and OKTO8. OKTO0 and OKTO8 were chosen because of their innate representation of GOOD and POOR members, while OKTO4 and OKTO5 were chosen because of the divergence occurring between these solutions.

The sensitivity experiments with respect to cold pools included WRF simulations with all latent heating turned off in the microphysics (“fake dry”) for the full 24-h period, latent heating of vaporization turned off in the microphysics (“no latent vaporization”) for the full 24-h period, and the same fake-dry and no latent vaporization experiments but only turning off the respective microphysics components at 0100 UTC 10 June just prior to solution divergence. This was done for OKTO0, OKTO4, OKTO5, and OKTO8. Figure 13 shows the OKTO4 fake dry and no latent vaporization restart runs at 0200 UTC 10 June and 0300 UTC 10 June, 1 and 2 h after turning off the respective portion of the microphysics. The evolution of OKTO4 is identical from 1200 UTC 9 June to 0100 UTC 10 June, and can be tracked until 0200 UTC 10 June in the first row of Fig. 12. Comparing 0200 UTC 10 June and 0300 UTC 10 June from Figs. 12 and 13, it can be seen that turning off the latent heating (either all latent heating or just from vaporization; not shown) has the same effect, preventing the

¹ The recent study of Wang et al. (2012) showed that error growth in warm-season moist convection is independent of the complexity of the microphysics parameterization schemes used in WRF.

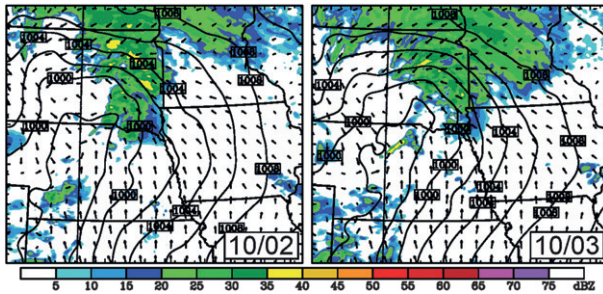


FIG. 13. Simulated radar reflectivity (shaded every 5 dBZ), sea level pressure (contoured every 2 hPa), and surface wind vectors at 0200 and 0300 UTC 10 Jun: for the OKTO4 fakedry experiment with all latent heating disabled at 0100 UTC 10 Jun.

development of the southern squall line. The same was true with OKTO0 (not shown). Turning off all heating or just from vaporization causes all four members to have minimal reflectivity in the northern portion of D04, with no convection in the southern portion (OKTO0, OKTO5, and OKTO8 not shown). These experiments support the hypothesis that the cold pools associated with the convection moving out of northeastern Colorado are a factor in OKTO4 and related GOOD members in generating a squall line in the southern portion of the domain.

Experiments on the effect of the large-scale forcing were performed through switching the initial conditions of the two outer domains (D01 and D02, which are used as boundary conditions for the two innermost domains, D03 and D04) between OKTO4 and OKTO5. Examining the OKTO4 with OKTO5 BCs and vice versa showed similar results as not switching the boundary conditions from the two outer domains. These two sensitivity experiments suggest that the larger-scale forcing during the developing phase of the convection out of northeastern Colorado is not the leading cause of the divergence between OKTO4 and OKTO5 (though it does contribute to small environmental differences).

Figure 14 portrays simulated environmental soundings at Grant (Fig. 14a) and North Platte, Nebraska (Fig. 14b), at 2200 UTC 9 June, the time convection begins approaching the Colorado–Nebraska border, for OKTO0, OKTO4, OKTO5, and OKTO8. The sounding in Fig. 14a is on the western side of the surface trough, relative to each member except for OKTO8. The spatial dislocation of the upper-level trough and corresponding surface low is located farther west for OKTO8 (the POOR flow regime). The remaining members have very similar environments with minimal differences in moisture, wind, and temperature profiles. Figure 14b is on the eastern side of the surface trough, with OKTO0 having a slightly warmer and drier boundary layer and OKTO0 and

OKTO4 having slightly stronger shear. It is clear that the cascading effect of the upper-level trough has an effect on the environment for each member, changing the spatial location of the surface trough and associated moisture, temperature, and wind profiles.

This dislocation of the environments is shown in Fig. 15 for the OKTO4 – OKTO5 difference in 100-m CAPE (Fig. 15a), 0–6-km wind shear (Fig. 15b), and 3-km relative humidity (Fig. 15c) with the actual respective field values for OKTO4 contoured. The trough axis is clearly seen in all three difference fields associated with the farther westward displacement of the surface trough in OKTO5. The environmental conditions are similar on either side of the trough for OKTO4 and OKTO5, seen in Figs. 14a and 14b. Relative to the convection moving out of northeastern Colorado and the associated cell that develops a stronger cold pool in OKTO4, the cell encounters higher CAPE, higher 0–6-km shear, and higher 3-km midlevel relative humidity in OKTO5 compared with OKTO4 due to this displacement. The complexity of the environmental differences at the time of cell divergence allows only speculation that the slight displacement west of the surface trough aids in the weakening of the cell in OKTO5 and an associated weaker cold pool. The midlevel moisture in OKTO5 is marginally higher farther west when cold pool differences develop (cells at points A and B in Fig. 12 at 0100 UTC 10 June) compared with OKTO4. With the convective triggering at this point being a function of marginal differences, the cell in OKTO4 has a favorable setup to trigger convection on the eastern side of the surface trough and organize into the southern portion of the squall line.

c. Error growth in terms of DTE

Further examination of the error growth dynamics in the sensitivity simulations is performed in terms of the RMDTE. The horizontal RMDTE is shown in Fig. 16, and the vertical RMDTE is shown in Fig. 10c for the differences between OKTO4 and OKTO5 from 1200 UTC 9 June to 1200 UTC 10 June. Comparing the horizontal and vertical RMDTE with those in Figs. 9 and 10a, respectively, the error growth of OKTO4 and OKTO5 is in strong agreement with the error growth of the entire original ensemble. The horizontal RMDTE in Fig. 16 shows a smaller domain-average initial error at 1200 UTC 9 June ($\sim 0.5 \text{ m s}^{-1}$) compared with that of the entire 40-member ensemble ($\sim 2\text{--}3 \text{ m s}^{-1}$). The error growth is consistent with the differences in convection over central Kansas by the middle of the simulation and the large error growth by the end of the simulation due to a lack of southern squall line development in OKTO5. The similar evolution of RMDTE of OKTO4 and OKTO5 to that of the entire ensemble suggests that OKTO4 and OKTO5

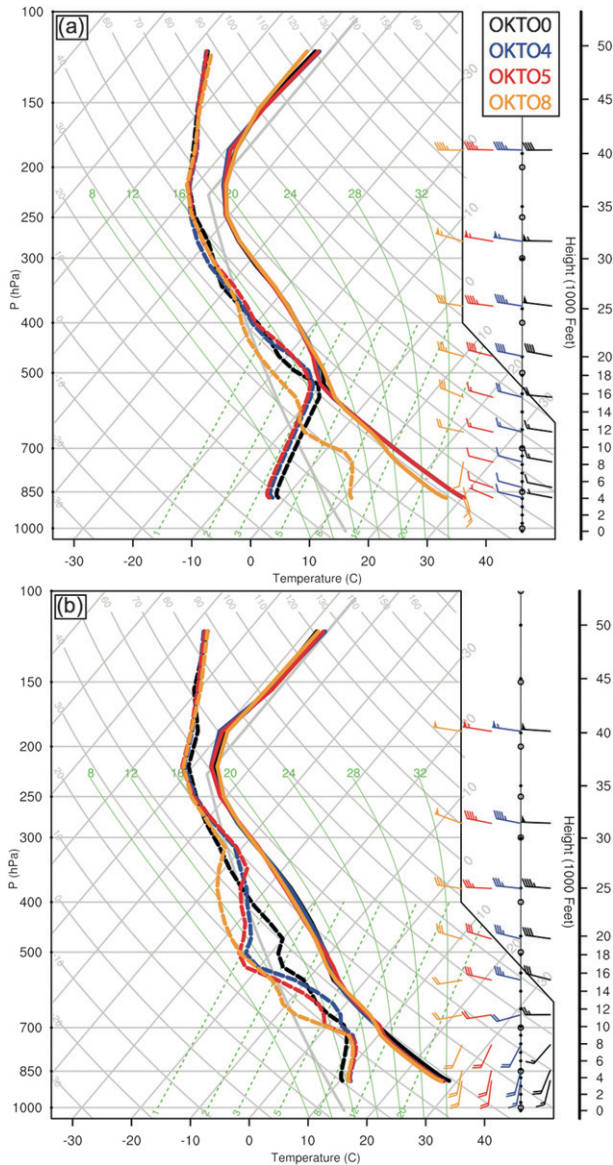


FIG. 14. Environmental soundings for OKTO0 (black), OKTO4 (blue), OKTO5 (red), and OKTO8 (yellow) at 2200 UTC 9 Jun at (a) Grant and (b) North Platte, NE. The locations of the soundings are indicated in Fig. 15c: (a) west star sounding and (b) east star sounding.

may retain many of the important features and error evolution features as the entire ensemble. It is interesting to note that even though the initial condition RMDTE difference for OKTO4 and OKTO5 is nearly an order of magnitude smaller than the initial ensemble, by 0900 UTC 10 June the RMDTE differences are almost identical in magnitude, exemplifying the nonlinearity of forecast error growth under moist dynamics.

Figure 17a displays the power spectra of the domain total DTE for OKTO1 – OKTO2, OKTO4 – OKTO5,

and OKTO7 – OKTO8 at 0000 UTC 10 June (after convective initiation) and at 0900 UTC 10 June during the 24-h forecast period. The three pairs of runs represent when the initial conditions of each forecast lie predominantly in the GOOD regime (OKTO1 – OKTO2), encompass the bifurcation point (OKTO4 – OKTO5), and in the POOR regime (OKTO7 – OKTO8). Comparing the three instances at the initial forecast time indicates the error is initially consistent throughout all wavelengths. Only after the convection evolves does the error saturate at the small scales [$O(10\text{ km})$] and cascade to the larger scales. The upscale cascade is evident at 0900 UTC 10 June with a larger total DTE for the bifurcating instance (OKTO4 – OKTO5). The distribution of total DTE is about 3–5 times larger at the subsynoptic scales (wavelengths $\geq 100\text{ km}$) than the GOOD regime instance (OKTO1 – OKTO2). The total DTE for OKTO0 – OKTO1 increases minimally at the largest wavelengths on the plot, indicating the errors have yet to affect these wavelengths.

Figure 17b displays the time evolution of the total DTE between OKTO0 and OKTO8, and various pairs of the sensitivity experiment members. In terms of total DTE, the initial difference between OKTO4 and OKTO5 will be one-sixty-fourth, nearly two orders of magnitude less than the OKTO0 – OKTO8 at 1200 UTC 9 June. In comparing the final total DTE at 1200 UTC 10 June of OKTO0 – OKTO8 to the subsequent pairs of experiments with decreasing smaller initial differences (e.g., OKTO0 – OKTO4, OKTO0 – OKTO2), reducing the initial condition error does lead to reduced final DTE and thus improves the predictability, but at a decreasing rate. Once the initial condition difference has been reduced to one-fourth (e.g., OKTO0 – OKTO2), further reduction minimally improves the predictability (e.g., OKTO3 – OKTO4, OKTO4 – OKTO5). The difference between the initial and final DTE is nonlinear, and each simulated reduction in initial condition error produces a smaller percentage of reduction in the final DTE. After reducing to one-eighth the difference between OKTO0 and OKTO8, further reductions minimally impact the predictability, except for the two extreme pairs (OKTO0 – OKTO1 and OKTO7 – OKTO8) in the same respective flow regimes. These sensitivity runs have similar solutions, and further reductions converge toward similar OKTO0 and OKTO8 solutions.

The increasing trend in total DTE between each pair of forecasts is hypothesized to be driven by the upscale error growth from moist processes and from the injection of mesoscale-to-subsynoptic-scale flow differences from D02 as the trough enters D04. At 1800 UTC 9 June, a divergence occurs between the total DTE encompassing the GOOD (OKTO0 – OKTO4, OKTO0 – OKTO3,

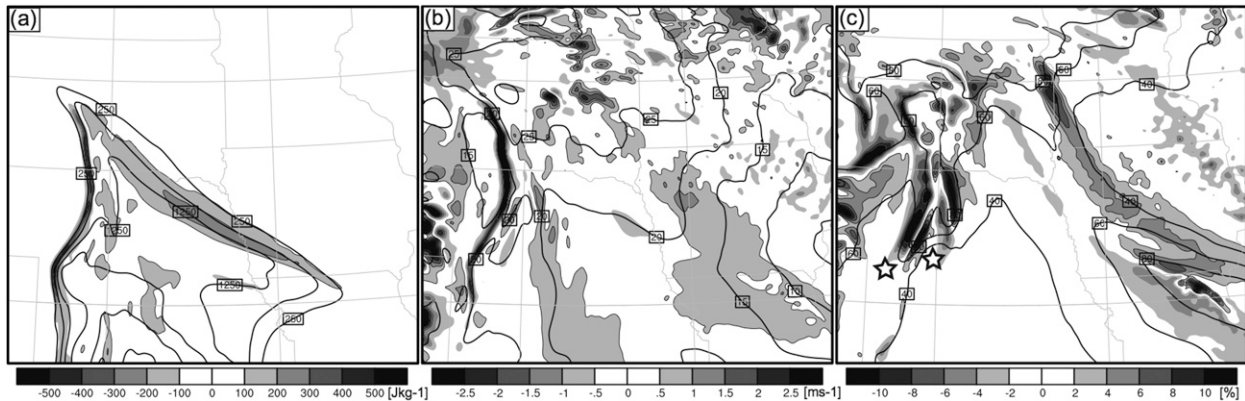


FIG. 15. Difference fields for OKTO4 – OKTO5 at 2200 UTC 9 Jun highlighting the spatial dislocation of environmental (a) CAPE (difference shaded every 250 J kg^{-1} , positive contoured; OKTO4 CAPE contoured every 500 J kg^{-1} starting at 250 J kg^{-1}); (b) 0–6-km shear (difference shaded every 0.5 m s^{-1} , positive contoured; OKTO4 0–6-km shear contoured every 5 m s^{-1}); and (c) 3-km relative humidity (difference shaded every 2%, positive contoured, and OKTO4 3-km relative humidity contoured every 20%).

etc.) and POOR (OKTO5 – OKTO8, OKTO6 – OKTO8, etc.) members surmised to be caused by a convective response to the stronger trough of the GOOD members entering D04. The total DTE drastically increases from 2200 UTC 9 June to 0000 UTC 10 June in response to convective initiation over south-central South Dakota. The simulations that form linear features (OKTO0 through OKTO4 and their associated total DTE analyses) exhibit a larger increase in total DTE due to enhanced deep convection. The simulations that do not form linear features (OKTO5 through OKTO8 and their associated total DTE analyses) produce less convection and therefore less variability in total DTE. An artificial decrease in the total DTE exists after 1000 UTC 10 June for all total DTE solutions due to convection exiting the domain, not because of any changes in mesoscale or convective features.

Focusing more closely on the bifurcating simulations described earlier (OKTO4 and OKTO5), the total DTE begins to rapidly increase by 0100 UTC 10 June. This increase is the result of OKTO4 developing a more pronounced squall line, whereas OKTO5 remains less convectively active to the south. The drastic total DTE increase further supports the increased convection in the southern domain, with the timing coinciding with the bifurcation of the convective development triggered by convective cells from northeastern Colorado in OKTO4 but not in OKTO5.

6. Schematic depiction of the intrinsic-versus-practical predictability

Figure 18 displays a schematic of the practical and intrinsic predictability inherent in this study due to reducing the initial condition uncertainties, similar to the sensitivity

experiments between OKTO0 and OKTO8. The circles represent the initial ensemble spread from the analysis, with the ensemble mean in the center (white dot) and the individual ensemble members (black dots) scattered around the ensemble mean. A larger circle represents a larger uncertainty in the initial conditions. Two specific simulation outcomes are indicated, a squall line forming (solid shading) and a non-squall line forming (striped pattern), although in general more than two possible outcomes for a forecast could exist. The progressively smaller circles represent smaller uncertainty in the initial conditions, achieved by decreasing the error in the analysis through better observations or better data assimilation. This was simulated in this study by averaging the initial differences of the GOOD regime and POOR regime members, that is, OKTO0 and OKTO8 to produce OKTO4, etc. The truth in Figs. 18a and 18b is indicated by a white cross and is assumed to always lie within the initial condition ensemble spread (as shall be the case for a well-behaved ensemble).

The 9–10 June 2003 squall line and bow echo observation (truth) falls predominantly within the GOOD (squall line forming) regime of the two flow regimes evident in the ensemble. Based on the sensitivity study, reducing the error in the initial conditions past current realistic levels may trend the ensemble members toward the GOOD flow regime solution and increase the practical predictability. Figure 11 clearly displays this trend with the observed squall line similar to OKTO0. By reducing the initial condition difference from OKTO4 to OKTO1, incremental improvement in the practical predictability was observed. This is displayed in Fig. 18a with the smaller circles in the GOOD regime forecast outcome representing the reduction in error for the initial conditions.

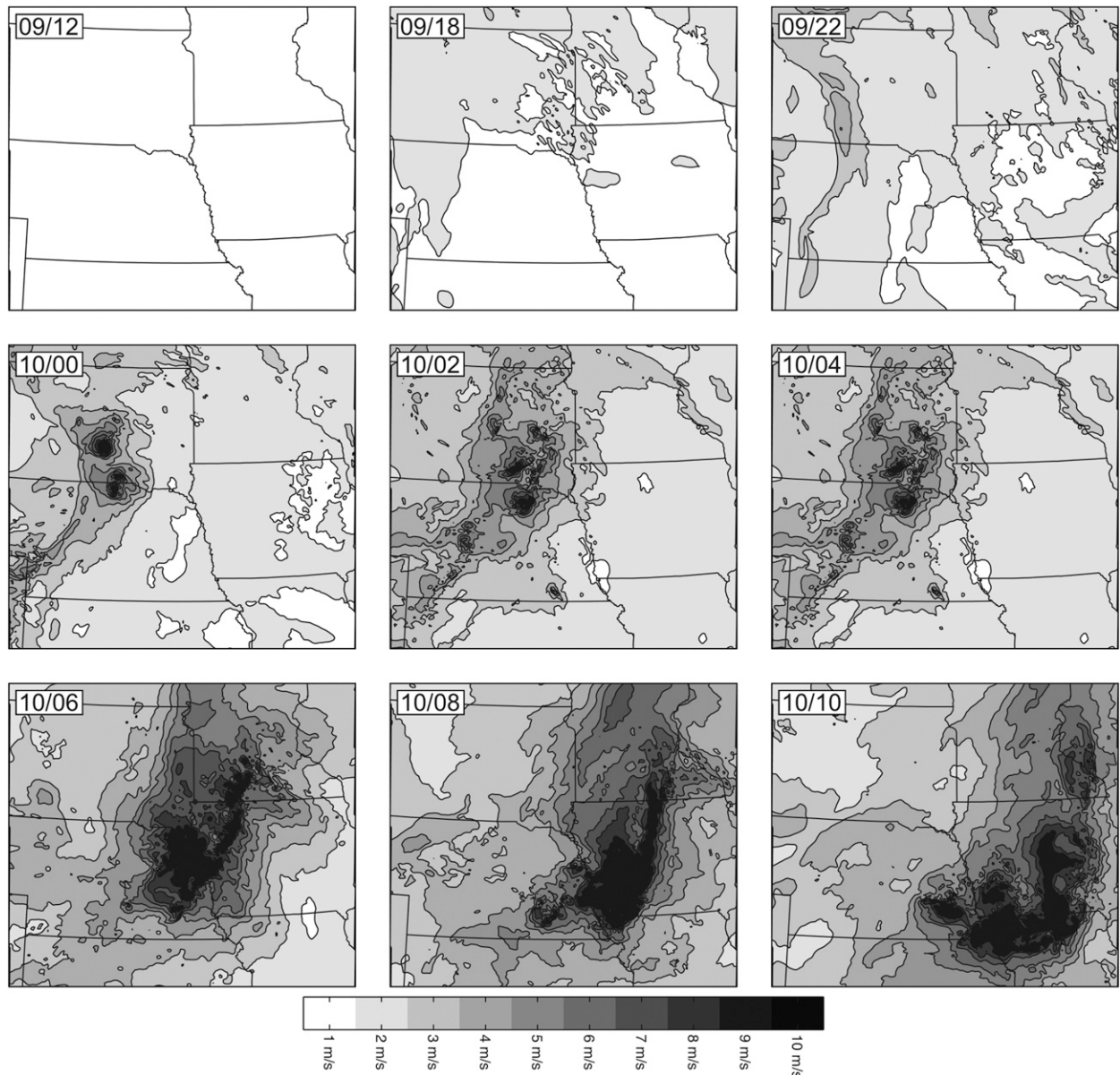


FIG. 16. Horizontal RMDTE showing the ensemble spread of OKTO4, OKTO5, and the full ensemble member average shaded (every 1 m s^{-1}) from 1200 UTC 09 Jun 2003 to 1000 UTC 10 Jun 2003.

If this same reduction in initial condition error is performed when the ensemble forecast outcome has equally favorable divergent solutions (i.e., having a similar number of solutions in both flow regimes as seen in Fig. 11 between OKTO4 and OKTO5), then decreasing the initial condition error will continue to have solutions for both GOOD and POOR regimes. In this case, no matter how much the error in the initial conditions is reduced, the ensemble will continue to embody both flow regimes (Fig. 18b) and the forecast accuracy will suffer.

On average over an extended period, if a reduction in error of the initial conditions is performed when the ensemble solutions favor a dominant flow regime, then an improvement in the averaged forecast accuracy (practical predictability) will occur. The amount of improvement depends on the flow characteristics of the forecast. The intrinsic predictability is highly forecast and flow dependent. If a dominant solution is not present, then little improvement in the averaged forecast accuracy will occur by further reducing the initial condition error.

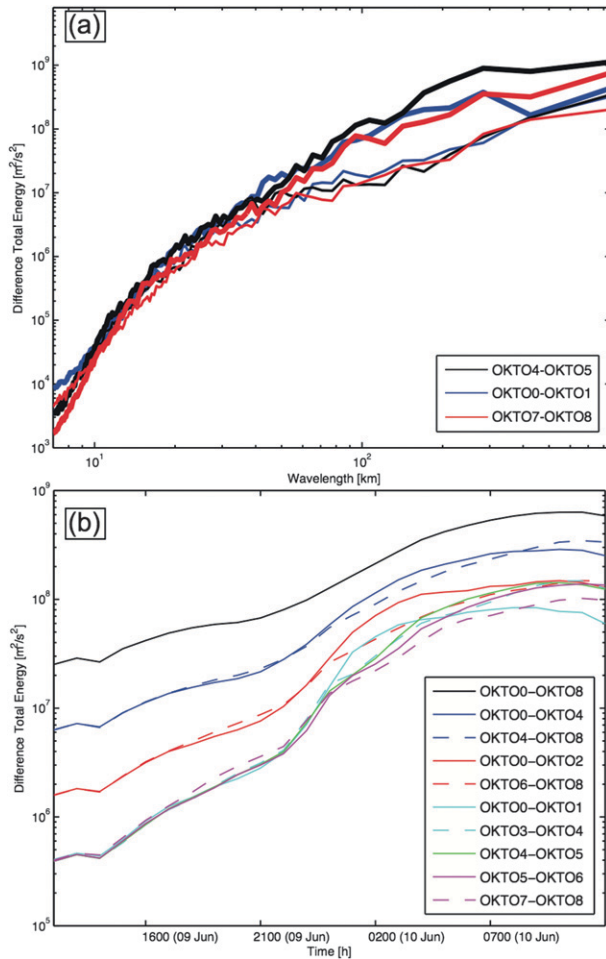


FIG. 17. (a) Power spectra of domain-integrated DTE ($m^2 s^{-2}$) (horizontal and vertical summation of DTE) between indicated simulations 0000 UTC 10 Jun (thin lines) and 0900 UTC 10 Jun (thick lines). (b) Time evolution of DTE ($m^2 s^{-2}$) between indicated simulations from 1200 UTC 9 Jun to 1200 UTC 10 Jun.

The schematic depicted in Fig. 18 is complementary to the findings of Palmer (1993), who eloquently depicted the loss of predictability during regime transition in nonlinear dynamic systems exemplified by the toy model of Lorenz (1963). Predicting the outcome of the nonlinear dynamic system is highly dependent on the state of the system and if it is near a regime change. For further information on the regime transition for a simplified model, the reader is encouraged to review Palmer (1993).

7. Summary and discussion

In this study, an ensemble of convection-permitting WRF forecasts initialized with perturbations from an EnKF analysis is used to explore the predictability of a bow echo event during BAMEX on 9–10 June 2003.

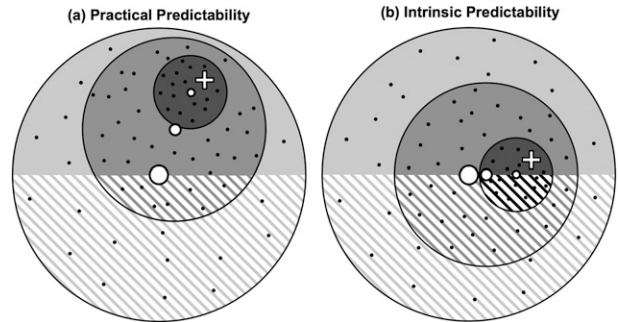


FIG. 18. Idealized schematic illustrating the reduction of initial-condition error by reducing the ensemble spread highlighting the (a) practical predictability representative of the 9–10 Jun 2003 squall line and bow echo and (b) intrinsic predictability representative of a theoretical ensemble forecast with the ensemble forecast having equally favorable solutions. Solid shading—flow regime 1; striped pattern—flow regime 2; black dots—ensemble members; white dots—ensemble mean; white cross—forecast truth.

The limit of practical predictability for this case may have been attained, shown by the large variability in evolution, mode, and flow regime. Subjectively choosing members defining two distinct storm development modes allows for the analysis of initial-condition spread on final storm development. Reducing initial-condition uncertainties and performing simulations within specific regimes highlight the intrinsic predictability.

The ensemble had considerable variability—some members developed strong squall lines and bow echoes that resembled observations, whereas other members had no southern squall line development. This variability was confirmed by a temporal analysis of RMDTE for the ensemble, with the greatest error growth caused by convective differences. Moist processes occurring with convection were the main contributor to differences between ensemble members.

The realistic initial condition uncertainties for the ensemble, produced by the EnKF analysis, were smaller than the FNL GFS and WRF 3DVar analyses run concurrently for this same case (Meng and Zhang 2008a,b), highlighting the practical predictability inherent in the current level of initial condition accuracy. The divergence of the members into two separate storm modes indicates the dependence of each ensemble member on the flow regime.

Using a perfect model assumption made in conjunction with initial condition uncertainties an order of magnitude smaller than the current observational analysis, the intrinsic predictability of the storm was analyzed. Ten squall-line-forming and 10 non-squall-line-forming ensemble members were subjectively chosen and their initial conditions averaged. The GOOD and POOR initial condition averages were again averaged to linearly reduce

the initial condition difference between the dominant flow regimes by one-half, one-quarter, and one-eighth and subsequently integrated for 24 h. A bifurcation of forecasts was evident within the linearly reduced forecasts, suggesting an intrinsic predictability limit for this case.

The environments of the developing and nondeveloping members evolved differently throughout the forecast period, caused by a dislocation of the upper-level trough and surface low. The resulting spatial difference in the surface trough and associated environments coupled with a triggering difference of the southern squall line aided by cold pool development of convection prior to squall line formation caused regime divergence. The cold pool development, strength, and spatial extent differed slightly due to the upscale error growth associated with deep moist convection moving out of northeastern Colorado. These differences coupled with environmental differences aided in the triggering of convection after passing through the surface trough for developing members producing a southern squall line, whereas the nondeveloping squall line.

The study of the predictability shows that the predictability is highly case and flow dependent. Improving the initial conditions can improve the practical predictability and forecast accuracy, with the solutions converging to a single solution when a dominant flow regime is evident in the ensemble forecast. The intrinsic predictability is highly flow dependent and if a dominant solution is not present, little improvement in the averaged forecast accuracy will occur by further reducing the initial condition error.

The domain-integrated DTE showed that improving the initial conditions by reducing the spread between members does not linearly decrease the final domain-integrated DTE. The response is nonlinear and a point is reached at which decreasing the initial-condition spread does not improve the predictability of the event, except when the correct flow regime is forecast.

The ensemble forecast and sensitivity experiments demonstrate that this storm has a practical limit in its predictability given realistic initial-condition uncertainties and that forecasts can be improved with more accurate and precise initial conditions coupled with an ensemble of forecasts using a reliable forecast model with sufficient grid resolutions. However, it is possible that the true storm could be near the point of bifurcation, where our predictive skill is intrinsically limited. In other words, we may be approaching the limit of intrinsic predictability for such an event due to the chaotic nature of moist convection. Future studies will aim to generalize this single case study to other severe convective weather and to explore the dependence of predictability under different flow regimes.

Acknowledgments. The authors benefited greatly from discussions with Morris Weisman, David Jorgensen, Jim Doyle, Yvette Richardson, Paul Markowski, Meng Zhang, and Yonghui Weng. The research is partially supported by National Science Foundation Grant AGS-0840651 and Office of Naval Research Grants N000140410471 and N000140910526.

REFERENCES

- Bei, N., and F. Zhang, 2007: Impacts of initial condition errors on mesoscale predictability of heavy precipitation along the mei-yu front of China. *Quart. J. Roy. Meteor. Soc.*, **133**, 83–99.
- Bryan, G., J. Wyngaard, and J. Fritch, 2003: Resolution requirements for the simulation of deep moist convection. *Mon. Wea. Rev.*, **131**, 2394–2416.
- Clark, A. J., W. A. Gallus Jr., M. Xue, and F. Kong, 2010: Growth of spread in convection-allowing and convection-parameterizing ensembles. *Wea. Forecasting*, **25**, 594–612.
- Davis, C., and Coauthors, 2004: The Bow Echo and MCV Experiment: Observations and opportunities. *Bull. Amer. Meteor. Soc.*, **85**, 1075–1093.
- Done, J., C. Davis, and M. Weisman, 2004: The next generation of NWP: Explicit forecasts of convection using the Weather Research and Forecasting (WRF) model. *Atmos. Sci. Lett.*, **5**, 110–117.
- Grell, G. A., and D. Dévényi, 2002: A generalized approach to parameterizing convection combining ensemble and data assimilation techniques. *Geophys. Res. Lett.*, **29**, 1693, doi:10.1029/2002GL015311.
- Hawblitzel, D., F. Zhang, Z. Meng, and C. Davis, 2007: Probabilistic evaluation of the dynamics and predictability of the mesoscale convective vortex of 10–13 June 2003. *Mon. Wea. Rev.*, **135**, 1544–1563.
- Hohenegger, C., and C. Schär, 2007a: Atmospheric predictability at synoptic versus cloud-resolving scales. *Bull. Amer. Meteor. Soc.*, **88**, 1783–1793.
- , and —, 2007b: Predictability and error growth dynamics in cloud-resolving models. *J. Atmos. Sci.*, **64**, 4467–4478.
- Hong, S., J. Dudhia, and S. Chen, 2004: A revised approach to ice microphysical processes for the bulk parameterization of clouds and precipitation. *Mon. Wea. Rev.*, **132**, 103–120.
- Lorenz, E. N., 1963: Deterministic nonperiodic flow. *J. Atmos. Sci.*, **20**, 130–141.
- , 1969: Atmospheric predictability as revealed by naturally occurring analogues. *J. Atmos. Sci.*, **26**, 636–646.
- , 1996: Predictability—A problem partly solved. *Proc. Seminar on Predictability*, Reading, United Kingdom, ECMWF, 1–18.
- Mapes, B. E., S. Tulich, T. Nasuno, and M. Satoh, 2008: Predictability aspects of global aqua-planet simulations with explicit convection. *J. Meteor. Soc. Japan*, **86A**, 175–185.
- Meng, Z., and F. Zhang, 2008a: Test of an ensemble Kalman filter for mesoscale and regional-scale data assimilation. Part III: Comparison with 3DVar in a real-data case study. *Mon. Wea. Rev.*, **136**, 522–540.
- , and —, 2008b: Test of an ensemble Kalman filter for mesoscale and regional-scale data assimilation. Part IV: Comparison with 3DVar in a month-long experiment. *Mon. Wea. Rev.*, **136**, 3671–3682.
- Noh, Y., W. Cheon, S. Hong, and S. Raasch, 2003: Improvement of the K-profile model for the planetary boundary layer based on large eddy simulation data. *Bound.-Layer Meteor.*, **107**, 401–427.

- Palmer, T. N., 1993: Extended-range atmospheric prediction and the Lorenz model. *Bull. Amer. Meteor. Soc.*, **74**, 49–65.
- Sellwood, K. J., S. Majumdar, B. Mapes, and I. Szunyogh, 2008: Predicting the influence of observations on medium-range forecasts of atmospheric flow. *Quart. J. Roy. Meteor. Soc.*, **134**, 2011–2027.
- Sippel, J., and F. Zhang, 2008: A probabilistic analysis of the dynamics and predictability of tropical cyclogenesis. *J. Atmos. Sci.*, **65**, 3440–3459.
- , and —, 2010: Factors affecting the predictability of Hurricane Humberto (2007). *J. Atmos. Sci.*, **67**, 1759–1778.
- Skamarock, W. C., J. B. Klemp, J. Dudhia, D. O. Gill, D. M. Barker, W. Wang, and J. G. Powers, 2005: A description of the Advanced Research WRF version 2. NCAR Tech. Note NCAR/TN-468+STR, 88 pp.
- Tan, Z., F. Zhang, R. Rotunno, and C. Snyder, 2004: Mesoscale predictability of moist baroclinic waves: Experiments with parameterized convection. *J. Atmos. Sci.*, **61**, 1794–1804.
- Wandishin, M. S., D. J. Stensrud, S. L. Mullen, and L. J. Wicker, 2008: On the predictability of mesoscale convective systems: Two-dimensional simulations. *Wea. Forecasting*, **23**, 773–785.
- , —, —, and —, 2010: On the predictability of mesoscale convective systems: Three-dimensional simulations. *Mon. Wea. Rev.*, **138**, 863–885.
- Wang, H., T. Auligné, and H. Morrison, 2012: Impact of microphysics scheme complexity on the propagation of initial perturbations. *Mon. Wea. Rev.*, **140**, 2287–2296.
- Weisman, M. L., and J. B. Klemp, 1982: The dependence of numerically simulated convective storms on wind shear and buoyancy. *Mon. Wea. Rev.*, **110**, 504–520.
- Zhang, F., 2005: Dynamics and structure of mesoscale error covariance of a winter cyclone estimated through short-range ensemble forecasts. *Mon. Wea. Rev.*, **133**, 2876–2893.
- , and J. Sippel, 2009: Effects of moist convection on hurricane predictability. *J. Atmos. Sci.*, **66**, 1944–1961.
- , C. Snyder, and R. Rotunno, 2002: Mesoscale predictability of the surprise snowstorm of 24–25 January 2000. *Mon. Wea. Rev.*, **130**, 1617–1632.
- , —, and —, 2003: Effects of moist convection on mesoscale predictability. *J. Atmos. Sci.*, **60**, 1173–1185.
- , A. Odins, and J. W. Nielsen-Gammon, 2006: Mesoscale predictability of an extreme warm-season rainfall event. *Wea. Forecasting*, **21**, 149–166.
- , N. Bei, R. Rotunno, C. Snyder, and C. Epifanio, 2007: Mesoscale predictability of moist baroclinic waves: Convection-permitting experiments and multistage error growth dynamics. *J. Atmos. Sci.*, **64**, 3579–3594.